Journal of Computational Physics 228 (2009) 3789–3815

Contents lists available at ScienceDirect

Journal of Computational Physics

journal homepage: www.elsevier.com/locate/jcp

A high-order numerical method for the nonlinear Helmholtz equation in multidimensional layered media

G. Baruch [a], G. Fibich [a], S. Tsynkov [b,*]

[a] Department of Applied Mathematics, School of Mathematical Sciences, Tel Aviv University, Ramat Aviv, Tel Aviv 69978, Israel
[b] Department of Mathematics, North Carolina State University, Box 8205, Raleigh, NC 27695, USA

ARTICLE INFO

Article history:
Received 2 October 2008
Received in revised form 9 February 2009
Accepted 10 February 2009
Available online 27 February 2009

Keywords:
Nonlinear optics
Kerr nonlinearity
Inhomogeneous medium
Material discontinuities
Discontinuous coefficients
Layered medium
Nonparaxiality
Forward scattering
Backscattering
(Narrow) solitons
Paraxial approximation
Nonlinear Schrödinger equation
Arrest of collapse
Finite-difference approximation
Compact scheme
High-order method
Artificial boundary conditions (ABCs)
Two-way ABCs
Traveling waves
Complex valued solutions
Frechét differentiability
Newton's method

ABSTRACT

We present a novel computational methodology for solving the scalar nonlinear Helmholtz equation (NLH) that governs the propagation of laser light in Kerr dielectrics.

The methodology addresses two well-known challenges in nonlinear optics: Singular behavior of solutions when the scattering in the medium is assumed predominantly forward (paraxial regime), and the presence of discontinuities in the optical properties of the medium. Specifically, we consider a slab of nonlinear material which may be grated in the direction of propagation and which is immersed in a linear medium as a whole. The key components of the methodology are a semi-compact high-order finite-difference scheme that maintains accuracy across the discontinuities and enables sub-wavelength resolution on large domains at a tolerable cost, a nonlocal two-way artificial boundary condition (ABC) that simultaneously facilitates the reflectionless propagation of the outgoing waves and forward propagation of the given incoming waves, and a nonlinear solver based on Newton's method.

The proposed methodology combines and substantially extends the capabilities of our previous techniques built for 1D and for multi-D. It facilitates a direct numerical study of nonparaxial propagation and goes well beyond the approaches in the literature based on the "augmented" paraxial models. In particular, it provides the first ever evidence that the singularity of the solution indeed disappears in the scalar NLH model that includes the nonparaxial effects. It also enables simulation of the wavelength-width spatial solitons, as well as of the counter-propagating solitons.

* Corresponding author. Tel.: +1 919 515 1877; fax: +1 919 513 7336.
E-mail addresses: guybar@tau.ac.il (G. Baruch), fibich@tau.ac.il (G. Fibich), tsynkov@math.ncsu.edu (S. Tsynkov).
URLs: http://www.tau.ac.il/~guybar (G. Baruch), http://www.math.tau.ac.il/~fibich (G. Fibich), http://www.math.ncsu.edu/~stsynkov (S. Tsynkov).

0021-9991/$ - see front matter © 2009 Elsevier Inc. All rights reserved.
doi:10.1016/j.jcp.2009.02.014

1. Introduction

1.1. Mathematical models

The propagation of electromagnetic waves in materials is governed by Maxwell's equations with appropriately chosen material responses. The responses characterize the dependence of material properties – magnetic permeability, electric permittivity, and conductivity – on the location and frequency of the propagating field. For high intensity radiation, the material quantities may also depend on the magnitude of the propagating field, which makes the responses nonlinear.

In nonlinear optics, one is often interested in studying the propagation of monochromatic waves (continuous-wave laser beams) through transparent dielectrics. In this case, the generation of higher harmonics and nonlinear coupling between different (temporal) frequencies can often be neglected, and accordingly, a time-harmonic solution can be assumed. The magnetic field can then be eliminated, and Maxwell's equations transform to a second-order differential equation with respect to the electric field, known as the vector Helmholtz equation, see [1]. If the material is isotropic and, in addition, the electric field is assumed linearly polarized, then one arrives at the scalar nonlinear Helmholtz equation (NLH):

$$\Delta E(\boldsymbol{x}) + \frac{\omega_0^2}{c^2} n^2 E = 0, \quad n^2(\boldsymbol{x}, |E|) = n_0^2(\boldsymbol{x}) + 2n_0(\boldsymbol{x}) n_2(\boldsymbol{x}) |E|^{2\sigma}, \tag{1}$$

where $\sigma > 0$ and n is the refraction index. In physical materials one always has $\sigma = 1$, so that the dependence of n^2 on $|E|$ is quadratic.

In Eq. (1), $\boldsymbol{x} = [x_1, \ldots, x_D]$ are the spatial coordinates, $E = E(\boldsymbol{x})$ denotes the scalar electric field, ω_0 is the laser frequency, c is the speed of light in vacuum, $\Delta = \partial_{x_1}^2 + \cdots + \partial_{x_D}^2$ is the D-dimensional Laplacian, n_0 is the linear index of refraction, and n_2 is the Kerr coefficient. Both n_0 and n_2 are assumed real, so that the medium is transparent or lossless.

The coordinate x_D will also be denoted by z and will hereafter be referred to as longitudinal, whereas the remaining direction(s) $\boldsymbol{x}_\perp = [x_1, \ldots, x_{D-1}]$ will be called transverse.

Our primary physical setup involves a slab of Kerr material surrounded on both sides by the linear homogeneous medium in which $n_0 \equiv n_0^{\text{ext}}$ and $n_2 \equiv 0$, see Fig. 1(a).

We introduce the linear wavenumber $k_0 = \omega_0 n_0^{\text{ext}}/c$ and the normalized quantities $v(\boldsymbol{x}) = n_0(\boldsymbol{x})/n_0^{\text{ext}}$ and $\epsilon(\boldsymbol{x}) = 2n_0(\boldsymbol{x}) n_2(\boldsymbol{x})/(n_0^{\text{ext}})^2$, and then recast Eq. (1) as

$$\Delta E(\boldsymbol{x}) + k_0^2 \Big(v^2(\boldsymbol{x}) + \epsilon(\boldsymbol{x}) |E|^{2\sigma} \Big) E = 0. \tag{2}$$

Note that the Kerr coefficient $n_2(\boldsymbol{x})$ is always discontinuous at the interface planes $z = 0$ and $z = Z_{\max}$, see Fig. 1(a). The linear index of refraction $n_0(x)$ may also be discontinuous at the interface planes. Discontinuities in $n_0(x)$ and $n_2(x)$ immediately give rise to those in $v(x)$ and $\epsilon(x)$, see Eq. (2). Thus, for the typical experimental setting that involves a slab of homogeneous Kerr material,[1] the coefficients of Eq. (2) are piecewise-constant:

$$v(z, x_\perp) = \begin{cases} 1, & z < 0, \\ v^{\text{int}}, & 0 \leqslant z \leqslant Z_{\max}, \\ 1, & z > Z_{\max}, \end{cases} \quad \text{and} \quad \epsilon(z, x_\perp) = \begin{cases} 0, & z < 0, \\ \epsilon^{\text{int}}, & 0 \leqslant z \leqslant Z_{\max}, \\ 0, & z > Z_{\max}. \end{cases} \tag{3}$$

Discontinuities in the coefficients (3) imply that additional conditions will be required for the NLH (2) at the interfaces $z = 0$ and $z = Z_{\max}$. These conditions can be obtained by analyzing the corresponding Maxwell's equations. They reduce to the continuity of the field $E(z)$ and its first normal derivative $\frac{\partial E}{\partial z}$, see Appendix A. When building a numerical approximation, the presence of material discontinuities requires special attention (Sections 2 and 3).

The problem is driven by a laser beam that impinges on the Kerr material from the outside and causes a local increase in the overall index of refraction as it propagates through, see Fig. 1(a). Since light rays bend toward the areas with higher refraction index, the impinging beam self-focuses inside the Kerr medium. The material discontinuities at $z = 0$ and $z = Z_{\max}$ reflect a portion of the forward propagating wave, resulting in backward propagating waves. Moreover, the nonlinearly induced nonuniformities of the refraction index may also scatter the radiation backwards. The presence of waves propagating in opposite directions implies that the boundary conditions for the NLH (2) must ensure the reflectionless propagation of all the outgoing waves (regardless of their direction of travel and the angle of incidence at the outer boundary) and at the same time correctly prescribe the given incoming beam at the boundary, see Fig. 2. Such boundary conditions are called *two-way boundary conditions* [2], see Section 2 for 1D and Section 3 for multi-D.

One can also consider a simplified model that would account only for the forward propagating component of the field. Let $z \equiv x_D$ be the direction of the impinging laser beam, and let us also consider the simplest case of $v \equiv 1$ and $\epsilon \equiv \epsilon^{\text{int}}$ inside the Kerr medium. Then, introducing the ansatz $E = e^{ik_0 z}\phi$, where $\phi = \phi(x)$ is assumed to vary slowly compared with the fast carrier oscillation $e^{ik_0 z}$, one can neglect the small ϕ_{zz} term (paraxial approximation), and reduce the NLH (2) to the nonlinear Schrödinger equation (NLS):

$$2ik_0 \phi_z(z, x_\perp) + \Delta_\perp \phi + k_0^2 \epsilon |\phi|^{2\sigma} \phi = 0, \quad 0 \leqslant z \leqslant Z_{\max}, \tag{4}$$

[1] This setup withstands an easy generalization to the case of multiple plane-parallel layers, see Section 1.3.

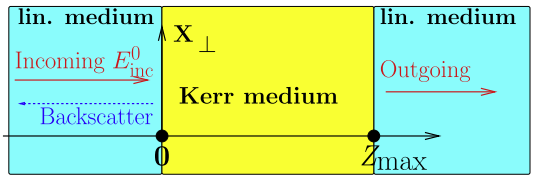

Fig. 1(a). The three-layer physical setup.

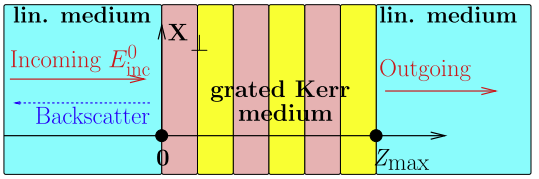

Fig. 1(b). The multi-layer physical setup.

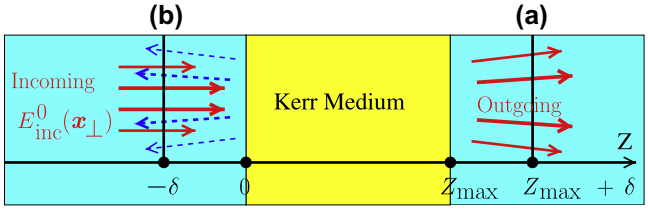

Fig. 2. Schematic of the boundary conditions in the longitudinal direction: (a) One-way radiation boundary condition at $z = Z_{\max} + \delta$; (b) Two-way radiation boundary condition at $z = -\delta$.

which governs the envelope ϕ. In Eq. (4), $\Delta_\perp = \partial^2_{x_1} + \cdots + \partial^2_{x_{D-1}}$ denotes the transverse Laplacian. The NLS (4) supports only forward propagation because the assumption of slow variation of ϕ does not leave room for any $\sim e^{-ik_0 z}$ components in the solution. Eq. (4) is first order in z and, unlike the NLH, requires a Cauchy problem to be formulated and solved with the "initial" data provided by the impinging wave and specified, say, at $z = 0$ (see, e.g., [3,4] for detail).

It is well known that solutions of the NLS (4) exist globally when $\sigma(D-1) < 2$, the subcritical NLS, but can become singular, i.e., collapse at finite propagation distances, when either $\sigma(D-1) > 2$, the supercritical NLS, or $\sigma(D-1) = 2$, the critical NLS [3].

As shown by Weinstein [5], a necessary condition for singularity formation in the critical NLS is that the input power exceeds the critical power P_c. The value of P_c is equal to the power of the ground-state solitary wave solution of the NLS; it can be calculated analytically for $D = 2$ and numerically for $D > 2$.

A question that has been open in the literature for over forty years is whether the more comprehensive NLH model for nonlinear self-focusing eliminates the singular behavior that characterizes collapsing solutions of the critical and supercritical NLS. Unfortunately, the fundamental issue of solvability of the NLH and regularity of its solutions still remains unaddressed for many important settings. Only the one-dimensional case, when Eq. (2) becomes an ODE, has been studied extensively, and exact solutions have been obtained using a combination of analytical and numerical means [6–13]. In multi-D, there have been indications that solutions of the NLH may exist even when the corresponding NLS solutions become singular, based on both numerical study of "modified" NLS equations [14–16], and on asymptotic analysis [17], but these studies did not account for backscattering. Recently, Sever employed a Palais–Smale type argument and has shown that the multi-D NLH is solvable in the sense of H^1 and that the solution is not unique [18]. His argument, however, only applies to self-adjoint operators, whereas the physical setups considered in this study require radiation boundary conditions.

1.2. Numerical method

The new computational methodology for the NLH that we present builds up on our previous work [19,2,20,21] and extends it substantially. We introduce a new semi-compact discretization and a new Newton's solver, and the ensuing capabilities include an explicit demonstration of the removal of singularity that "plagues" the NLS, and the computation of narrow nonparaxial solitons.

Specifically, we solve the NLH (2) for two different cases.

The first one corresponds to the critical NLS ($\sigma(D-1) = 2$). We consider both the two-dimensional quintic nonlinearity $D = 2$ and $\sigma = 2$ (planar waveguides), and the three-dimensional cubic nonlinearity $D = 3$ and $\sigma = 1$ (bulk Kerr medium, for

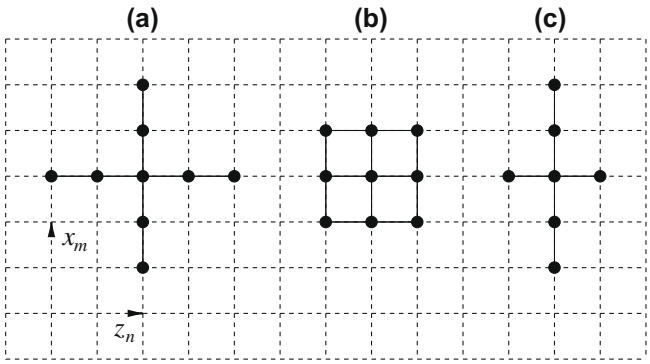

Fig. 3. Stencils in 2*D*: (a) Standard central difference fourth-order stencil, as in our previous work [2,20,21]; (b) Compact 3×3 fourth-order stencil for linear operators, as, e.g., in [23,24]; (c) Semi-compact stencil used in this work.

which we additionally assume cylindrical symmetry). As $\sigma(D-1)=2$ for either setting, one can expect that the role of nonparaxiality and backscattering will be similar.

This study goes beyond the investigation of the "modified" NLS's [14–17], and the results reported in Section 7.2 *provide the first ever numerical evidence that the collapse of focusing nonlinear waves is indeed arrested in the NLH model, which incorporates the nonparaxiality and backscattering.*

The second case we analyze is that of a planar waveguide with cubic nonlinearity ($D=2$ and $\sigma=1$). In this subcritical case, solutions to the NLS do not collapse. Instead, the laser beam can propagate in the Kerr medium over very long distances without changing its profile[2] – the type of behavior often referred to as spatial soliton. Solitons have been studied extensively as solutions to the NLS. For beams that are much wider than the optical wavelength, it is generally expected that the "subcritical" NLH will have similarly looking solutions. However, it was not until our paper [20] that it has become actually possible to study the effect of nonparaxiality and backscattering on solitons. The methodology proposed in this paper allows us to go further and demonstrate numerically *the existence and sustainability over long distances of very narrow spatial solitons for the NLH,* basically as narrow as one carrier wavelength $\lambda = 2\pi/k_0$, see Section 7.1. Furthermore, the NLH appears particularly well suited for modeling interactions between counter-propagating solitons, as a boundary value problem can naturally be formulated.

In the NLS framework, on the other hand, the two counter-propagating solitons will imply two opposite directions of marching.[3]

The discrete approximation of the NLH must be high order so as to minimize the number of points per wavelength required for solving Eq. (2) with sub-wavelength resolution on a large domain, and for resolving the small-scale phenomenon of backscattering against a background of the forward-propagating wave. It must also maintain its accuracy across the material discontinuities. As the geometry is simple, and the discontinuities are only in the longitudinal direction, we can approximate the NLH by finite differences on a rectangular grid. In the case $D=2$, it will be a Cartesian grid of coordinates (x,z). In the case $D=3$, we still want to have only two independent spatial variables and hence employ cylindrical symmetry. The NLH (2) is then approximated on the rectangular grid of cylindrical coordinates (ρ,z), where $\rho=(x^2+y^2)^{1/2}$. In doing so, the discontinuities that are confined to transverse planes will always be aligned with the grid.

In our work [2,20], we used the standard fourth-order central differences (five node stencil in each coordinate direction) to approximate the NLH (2) on a rectangular grid, see Fig. 3(a). While this approach works well in the regions of smoothness, it deteriorates to second-order accuracy in regions of material discontinuities. In the recent paper [19], we discretized the one-dimensional NLH with fourth-order accuracy using compact finite volumes and a three node stencil. This discretization handled the material discontinuities with no deterioration of accuracy and was also extended to higher orders in the linear case [25]. However, the extension of the scheme of [19] to multi-D is not straightforward. Therefore, in the current paper we adopt a hybrid approach. We use the standard fourth-order central differences in the transverse direction, and a compact fourth-order finite difference discretization on three nodes in the longitudinal direction, see Fig. 3(c).

The five node transverse stencil does not impair the accuracy because there are no discontinuities in that direction. The three node longitudinal part of the scheme is supplemented by one-sided differences that implement the required interface conditions at the points of discontinuity. In doing so, the compact stencil eliminates the need to use those special differences anywhere except at the discontinuities themselves. Another advantage of having a three node compact stencil in the longitudinal direction is that it leads to matrices with a narrower bandwidth.

The interior discretization is supplemented by nonlocal two-way artificial boundary conditions (ABCs) set at $z=-\delta$ and $z=Z_{\max}+\delta$, see Fig. 2, and by local radiation boundary conditions at the transverse far-field boundaries. The discrete ABCs

[2] In this case, self-focusing balances diffraction exactly.

[3] Counter-propagating beams have been simulated using two coupled NLSs [22], but this approach involves some approximations which are not needed in the NLH, and whose validity is unclear.

are similar to those of [20], but having a three node compact stencil greatly simplifies their construction because, unlike in the case of a five node stencil, there are no additional evanescent modes in the discretization, see Section 3.4.

The solver employed in [2,20,21] was of a fixed-point type. On the outer iteration loop, the nonlinearity in Eq. (2) was frozen, and a linear Helmholtz equation with variable coefficients was obtained. This linear equation was then solved iteratively on the inner loop, essentially by building a sequence of Born approximations [26].

This double-loop iterative method was shown to converge for (subcritical) solitons and for "mild" critical cases, but has never been able to produce convergent solutions for incoming beams that become singular in the NLS model.

In [19], we have demonstrated that the iterations' convergence in [2,20,21] breaks down far below the power threshold for non-uniqueness of the one-dimensional problem. This suggested that the convergence difficulties in [2,20,21] were not related to the loss of uniqueness by the solution [18,8], but rather to the deficiencies of the iteration scheme itself. The latter may be (partially) accounted for by the known convergence limitations of the Born approximations, because they can be interpreted as a Neumann series [27] for the corresponding integral operator [26, Section 13.1.4].

An alternative iteration proposed in [19] is based on Newton's method. As, however, the Kerr nonlinearity is Frechét non-differentiable for complex-valued E, for Newton's method to apply the NLH has to be recast as a system of two equations with real unknowns. The one-dimensional numerical experiments of [19] demonstrate robust convergence of Newton's iterations for a wide range of input powers. Therefore, in this paper we implement Newton's method for solving the multi-dimensional NLH (2), see Section 4. As shown in Section 7.2, the method converges for initial conditions that lead to singularity formation in the critical NLS model, for both $D = 2$ and $D = 3$.

1.3. Extension to the multi-layer case

Instead of having a homogeneous Kerr material in the nonlinear region as shown in Fig. 1(a), we can analyze the case of a layered (grated) material as shown in Fig. 1(b). In doing so, the linear material outside of the Kerr slab still remain homogeneous.

The corresponding extension of the mathematical model is straightforward. It amounts to introducing a fixed partition of the interval $[0, Z_{\max}]$:

$$0 = \tilde{z}_0 < \cdots < \tilde{z}_l < \cdots < \tilde{z}_L = Z_{\max}, \tag{5a}$$

so that the material characteristics are constant within each sub-interval:

$$v(z, x_\perp) \equiv \tilde{v}_l, \quad \epsilon(z, x_\perp) \equiv \tilde{\epsilon}_l \quad \text{for } z \in (\tilde{z}_l, \tilde{z}_{l+1}), \tag{5b}$$

whereas at the interfaces (5a) they may undergo jumps. Altogether, this leaves the coefficients of Eq. (2) piecewise constant in z.

The additional interface conditions required by Eq. (2) are the same as before – continuity of E and $\frac{\partial E}{\partial z}$ between the layers, see Appendix A.

1.4. Structure of the paper

In Section 2, we illustrate the main concepts of the continuous formulation and the discretization for the one-dimensional NLH. In Section 3, we describe the continuous formulation of the problem and the discretization for the two-dimensional Cartesian NLH and for the three dimensional NLH with cylindrical symmetry. In Section 4, we introduce Newton's solver for the resulting system of nonlinear equations on the grid. Section 5 provides a summary on the numerical method, Section 6 relates the input beams for the NLH and the corresponding NLS models, and Section 7 contains the results of simulations. Finally, Section 8 presents our conclusions and outlines directions for future work. Note also that some of the results shown hereafter were previously reported in [28]. That paper, however, did not contain any description of the numerical method.

2. The NLH in one space dimension

In this section we consider the one-dimensional NLH with constant material coefficients v^2 and ϵ for $0 < z < Z_{\max}$, which means that there are two discontinuities at $z = 0$ and $z = Z_{\max}$, but no discontinuities in the interior of the Kerr slab, see Fig. 1(a). In Section 2.1, we present the continuous formulation of the problem, and in Section 2.2 we introduce a compact discrete approximation. In Section 2.3, we briefly discuss the extension to the multi-layer case outlined is Section 1.3. This simple one-dimensional case illustrates the key ideas and notations that will be used later in the more complex multi-dimensional cases.

2.1. Continuous formulation

Consider a homogeneous slab of the Kerr material immersed in an infinite linear medium.

The propagation of the electric field is governed by the 1D NLH equation inside the Kerr material:

$$\frac{d^2E(z)}{dz^2} + k_0^2\left(v^2 + \epsilon|E|^{2\sigma}\right)E = 0, \quad 0 < z < Z_{\max} \tag{6a}$$

and by the linear Helmholtz equation outside the Kerr material:

$$\frac{d^2E(z)}{dz^2} + k_0^2 E = 0, \quad z < 0 \text{ or } z > Z_{\max}. \tag{6b}$$

At the material interfaces $z = 0$ and $z = Z_{\max}$, the field and its first derivative must be continuous [19]:

$$\begin{aligned} &E(0+) = E(0-), \quad \frac{dE}{dz}(0+) = \frac{dE}{dz}(0-), \\ &E(Z_{\max}+) = E(Z_{\max}-), \quad \frac{dE}{dz}(Z_{\max}+) = \frac{dE}{dz}(Z_{\max}-). \end{aligned} \tag{6c}$$

We consider the case of two incoming waves with known characteristics that travel toward the Kerr region $[0, Z_{\max}]$ from $z = -\infty$ to the right and from $z = +\infty$ to the left.[4] The overall field may also have scattered components, which are outgoing with respect to the domain $[0, Z_{\max}]$ and which are not known ahead of time. The general solution to Eq. (6b) outside $[0, Z_{\max}]$ is a superposition of the right-propagating wave $e^{ik_0 z}$ and the left-propagating wave $e^{-ik_0 z}$. Consequently, the field outside $[0, Z_{\max}]$ shall be sought for in the form:

$$E(z) = \begin{cases} E_{\text{inc}}^0 e^{ik_0 z} + C_1 e^{-ik_0 z}, & -\infty < z \leqslant 0, \\ C_2 e^{ik_0 (z - Z_{\max})} + E_{\text{inc}}^{Z_{\max}} e^{-ik_0 (z - Z_{\max})}, & Z_{\max} \leqslant z < \infty, \end{cases} \tag{7}$$

where E_{inc}^0 is a given amplitude of the incoming wave that travels to the right from $z = -\infty$ and impinges on the Kerr medium at $z = 0$, whereas C_1 is the amplitude of the outgoing wave traveling to the left toward $z = -\infty$, which is not known ahead of time.[5] Likewise, $E_{\text{inc}}^{Z_{\max}}$ is a given amplitude of the incoming wave that travels to the left from $z = +\infty$ and impinges on the Kerr medium at $z = Z_{\max}$, whereas C_2 is the amplitude of the outgoing right-traveling wave, which is not known ahead of time.

Representation (7) is to be enforced by the ABCs that should prescribe the given values of E_{inc}^0 and $E_{\text{inc}}^{Z_{\max}}$ and at the same time allow for the arbitrary values of C_1 and C_2.

In [19], we have set such ABCs precisely at the material interfaces, and have shown that they were given by the inhomogeneous Sommerfeld type relations:

$$\left(\frac{d}{dz} + ik_0\right) E\Big|_{z=0} = 2ik_0 E_{\text{inc}}^0, \quad \left(\frac{d}{dz} - ik_0\right) E\Big|_{z=Z_{\max}} = -2ik_0 E_{\text{inc}}^{Z_{\max}}.$$

In this paper, we set equivalent ABCs at a certain distance $\delta > 0$ away from the interfaces, see Fig. 2, and inside the linear regions:

$$\begin{aligned} &\left(\tfrac{d}{dz} + ik_0\right) E\big|_{z=-\delta} = 2ik_0 e^{-ik_0\delta} E_{\text{inc}}^0, \\ &\left(\tfrac{d}{dz} - ik_0\right) E\big|_{z=Z_{\max}+\delta} = -2ik_0 e^{-ik_0\delta} E_{\text{inc}}^{Z_{\max}}. \end{aligned} \tag{8}$$

As we shall see, the separation between the material interfaces $z = 0$ and $z = Z_{\max}$ and artificial boundaries $z = -\delta$ and $z = Z_{\max} + \delta$ simplifies the discretization of the problem, because the continuity conditions (6c) and the boundary conditions (8) can be discretized independently of each other, see Sections 2.2.2 and 2.2.3, respectively.

2.2. Discrete approximation

The one-dimensional problem (6a), (8) will be approximated using compact fourth-order finite differences. We first discuss the discrete approximation of Eqs. (6a) and (6b), then the approximation of the interface condition (6c), and finally the approximation of the two-way ABCs (8). In what follows, we introduce some notations that will be particularly helpful in multi-D.

We begin with setting up a uniform grid of $N + 7$ nodes on $[-\delta, Z_{\max} + \delta]$:

$$z_n = n \cdot h, \quad h = \frac{Z_{\max}}{N}, \quad n = -3, -2, \ldots, N+2, N+3, \tag{9}$$

so that

$$z_0 = 0, \quad z_N = Z_{\max}, \quad \delta = 3h.$$

We also denote by E_n and $P_n = |E_n|^{2\sigma} E_n$ the values of E and of $|E|^{2\sigma} E$ at the grid nodes z_n. Finally, we introduce a special notation D for central difference operators, with the order of accuracy in the superscript and the differentiation variables in the subscript. For example,

$$D_{zz}^{(2)} E \stackrel{\text{def}}{=} \frac{E_{n+1} - 2E_n + E_{n-1}}{h^2} = \left.\frac{d^2E}{dz^2}\right|_{z=z_n} + \mathcal{O}\left(h^2\right).$$

[4] Hereafter, we slightly generalize the schematic depicted in Fig. 2, in that we allow for incoming waves to impinge on *both* interfaces, at $z = 0$ and $z = Z_{\max}$.

[5] Physically, the left-traveling outgoing wave $C_1 e^{-ik_0 z}$ may have two sources: A portion of the right-traveling wave $E_{\text{inc}}^0 e^{ik_0 z}$ may get *scattered* to the left by the Kerr material slab, and a portion of the left-traveling wave $E_{\text{inc}}^{Z_{\max}} e^{-ik_0 z}$ may be *transmitted* through by the Kerr material slab. In the nonlinear problem, these phenomena are coupled and cannot be easily distinguished from one another.

2.2.1. Approximation of the equation

Inside the Kerr medium, i.e., for $n = 1, \ldots, N-1$, the material coefficients v^2 and ϵ are constant, and hence the field $E(z)$ is smooth. Using Taylor's expansion of the field, we obtain from the standard second-order central difference approximation:

$$D_{zz}^{(2)}E = \frac{E_{n+1} - 2E_n + E_{n-1}}{h^2} = \partial_{zz}E_n + \frac{h^2}{12}\partial_{zzzz}E_n + \mathcal{O}\left(h^4\right). \tag{10}$$

Then, recasting the one-dimensional NLH (6a) as

$$\partial_{zz}E_n = -k_0^2\left(v^2 + \epsilon|E_n|^{2\sigma}\right)E_n = -k_0^2(v^2E_n + \epsilon P_n),$$

we can approximate the term $\partial_{zzzz}E_n$ on the right-hand side of (10) with second-order accuracy as

$$\partial_{zzzz}E_n = D_{zz}^{(2)}\partial_{zz}E_n + \mathcal{O}\left(h^2\right) = -k_0^2D_{zz}^{(2)}\left(v^2E_n + \epsilon P_n\right) + \mathcal{O}\left(h^2\right).$$

This yields a compact fourth-order approximation for the second derivative:

$$\partial_{zz}E_n = D_{zz}^{(2)}E_n + \frac{h^2k_0^2}{12}D_{zz}^{(2)}\left(v^2E_n + \epsilon P_n\right) + \mathcal{O}\left(h^4\right).$$

Then, the resulting scheme for the one-dimensional NLH (6a) at the interior nodes reads:

$$D_{zz}^{(2)}E_n + k_0^2\left(1 + \frac{h^2}{12}D_{zz}^{(2)}\right)\left(v^2E_n + \epsilon P_n\right) = 0, \quad n = 1, \ldots, N-1. \tag{11}$$

This approach is sometimes called *an equation-based approximation* [24].

Outside the Kerr medium, i.e., for $n < 0$ and $n > N$, the foregoing derivation is repeated with $v^2 \equiv 1$ and $\epsilon \equiv 0$, which yields a compact fourth-order approximation of the linear Helmholtz equation (6b):

$$\left(1 + \frac{k_0^2h^2}{12}\right)D_{zz}^{(2)}E_n + k_0^2E_n = 0, n = -3, -2, -1 \quad \text{and} \quad n = N+1, N+2, N+3. \tag{12}$$

Note that Eq. (12) for the outermost grid nodes $n = -3$ and $n = N+3$ will involve the ghost values E_{-4} and E_{N+4}, respectively. These ghost values will be determined from the discrete two-way ABCs, see Section 2.2.3.

2.2.2. Approximation at the interfaces

At the material interfaces $z = 0$ and $z = Z_{\max}$ (i.e., grid nodes $n = 0$ and $n = N$) the discretized field is given by E_0 and E_N, respectively. Hence, the continuity of E at the interface is automatically guaranteed, and only the continuity of E_z, see formula (6c), requires special attention. The latter is enforced by approximating the derivatives at the interfaces with fourth-order one-sided finite differences. We again use the differential equation to eliminate one grid point from the one-sided stencil and reduce it from the conventional five nodes to four. While reducing the size of the stencil at the interface is not as important as in the interior and exterior of the Kerr material, numerical observations show that in some cases it may bring down the truncation error at the interface by a factor of two.

Using Taylor's expansion and the one-dimensional NLH (6a), we can write:

$$\begin{aligned}\left.\frac{dE}{dz}\right|_{z=0+} &= \frac{-85E_0 + 108E_1 - 27E_2 + 4E_3}{66h} - \frac{3h}{11}\left.\frac{d^2E}{dz^2}\right|_{z=0+} + \mathcal{O}\left(h^4\right) \\ &= \frac{-85E_0 + 108E_1 - 27E_2 + 4E_3}{66h} + \frac{3k_0^2h}{11}\left(v_{0+}^2E_0 + \epsilon_{0+}P_{0+}\right) + \mathcal{O}\left(h^4\right).\end{aligned}$$

Repeating the calculation for $E_z(0-)$ and equating the resulting approximations for $E_z(0-)$ and $E_z(0+)$, we have:

$$\frac{4E_{-3} - 27E_{-2} + 108E_{-1} - 170E_0 + 108E_1 - 27E_2 + 4E_3}{66h} + \frac{6hk_0^2}{11}\left(\frac{v_{0-}^2 + v_{0+}^2}{2}E_0 + \frac{\epsilon_{0-} + \epsilon_{0+}}{2}P_0\right) = 0. \tag{13}$$

Then, substituting $v_{0-} = 1$, $\epsilon_{0-} = 0$, $v_{0+} = v$ and $\epsilon_{0+} = \epsilon$, we obtain:

$$\frac{4E_{-3} - 27E_{-2} + 108E_{-1} - 170E_0 + 108E_1 - 27E_2 + 4E_3}{66h} + \frac{6hk_0^2}{11}\left(\frac{1+v^2}{2}E_0 + \frac{\epsilon}{2}P_0\right) = 0. \tag{14a}$$

A similar equation is obtained for the interface at $n = N$:

$$\frac{4E_{N-3} - 27E_{N-2} + 108E_{N-1} - 170E_N + 108E_{N+1} - 27E_{N+2} + 4E_{N+3}}{66h} + \frac{6hk_0^2}{11}\left(\frac{1+v^2}{2}E_N + \frac{\epsilon}{2}P_N\right) = 0. \tag{14b}$$

2.2.3. Two-way boundary conditions

At the exterior nodes $n < 0$ and $n > N$, the one-dimensional Helmholtz equation (6b) is approximated with fourth-order accuracy by the constant coefficient homogeneous difference equation (12). This equation can be recast as

$$\frac{E_{n+1} - 2E_n + E_{n-1}}{h^2} + k^2 = 0, \quad \text{where } k^2 = \frac{1}{1 + k_0^2 h^2/12} k_0^2. \tag{15}$$

The general solution of Eq. (15) is of the form $E_n = C_+ q^n + C_- q^{-n}$, where

$$q = r + i\sqrt{1 - r^2} \quad \text{and} \quad q^{-1} = r - i\sqrt{1 - r^2}$$

are roots of the corresponding characteristic equation $q^{-1} - 2/r + q = 0$, and $r = (1 - k^2 h^2/2)^{-1}$. These roots are complex conjugate and have unit magnitudes. Moreover, they satisfy $q = e^{ik_0 h}(1 + \mathcal{O}(h^5))$ and $q^{-1} = e^{-ik_0 h}(1 + \mathcal{O}(h^5))$. Hence, the discrete solution q^n approximates the right-going wave $e^{ik_0 nh} = e^{ik_0 z}$, and the discrete solution q^{-n} approximates the left-going wave $e^{-ik_0 nh} = e^{-ik_0 z}$, with fourth-order accuracy.

Consequently, the discrete counterpart of Eq. (7) is

$$E_n = \begin{cases} E_{\text{inc}}^0 q^n + C_1 q^{-n}, & -\infty < n \leqslant 0, \\ C_2 q^{n-N} + E_{\text{inc}}^{Z_{\max}} e^{-(n-N)}, & N \leqslant n < \infty. \end{cases} \tag{16}$$

Applying Eq. (16) at $n = -3$ and $n = -4$, we can eliminate the unknown constant C_1 and express the value of the field at the ghost node $n = -4$ as

$$E_{-4} = (q^{-1} - q) q^{-3} E_{\text{inc}}^0 + q E_{-3}. \tag{17a}$$

Likewise, applying Eq. (16) at $n = N + 3$ and $n = N + 4$, we obtain:

$$E_{N+4} = (q^{-1} - q) q^{-3} E_{\text{inc}}^{Z_{\max}} + q E_{N+3}. \tag{17b}$$

Relations (17a) provide a fourth-order accurate approximation to the boundary conditions (8) for $\delta = 3h$. Relation (17a) is substituted into Eq. (12) for $n = -3$ and relation (17b) is substituted into Eq. (12) for $n = N + 3$. This eliminates the ghost values from scheme (12) and closes the system of difference equations on the grid (9).

2.3. Extension to the multi-layer material

In the case of a grated Kerr material described in Section 1.3, there are additional discontinuity points defined by formula (5a).

The interface conditions at each discontinuity point $\tilde{z}$ are the same as at $z = 0$ and $z = Z_{\max}$:

$$E(\tilde{z}+) = E(\tilde{z}-), \qquad \frac{dE}{dz}(\tilde{z}+) = \frac{dE}{dz}(\tilde{z}-).$$

Hence, in the simple case when $\tilde{z}$ happens to be at one of the grid nodes, the discrete continuity condition at $\tilde{z}$ is given by the same expression as (13). If the discontinuity point does not coincide with any grid node, one can construct a separate uniform grid for each sub-interval, and the extension to the multi-layer case will then be straightforward.

3. The NLH in two and three space dimensions

3.1. Continuous formulation

Here, we build a continuous formulation for the case of a homogeneous slab of the Kerr material which occupies the region $0 \leqslant z \leqslant Z_{\max}$, see Fig. 1(a). As in the one-dimensional setting, we will later generalize the method to the multi-layer case, see Section 3.5.

We first consider the two-dimensional Cartesian geometry case $x \equiv (z, x)$. This case models the physical case of propagation in planar waveguides, where the dynamics in y can be neglected. In this case, the computational domain is truncated in the transverse direction to $x \in [-X_{\max}, X_{\max}]$. In the longitudinal direction, we truncate the computational domain at a certain distance δ from the interfaces, to $z \in [-\delta, Z_{\max} + \delta]$.

As before, the electric field is governed by the scalar NLH equation inside the Kerr medium (cf. Eq. (2)):

$$\begin{aligned} &E_{zz}(z,x) + E_{xx} + k_0^2\left(v^2 + \epsilon|E|^{2\sigma}\right)E = 0, \\ &(z,x) \in (0, Z_{\max}) \times [-X_{\max}, X_{\max}] \end{aligned} \tag{18a}$$

and by the linear Helmholtz equation outside the Kerr medium (where $v \equiv 1$ and $\epsilon \equiv 0$):

$$\begin{aligned} &E_{zz}(z,x) + E_{xx} + k_0^2 E = 0, \\ &(z,x) \in \{[-\delta, 0) \cup (Z_{\max}, Z_{\max} + \delta]\} \times [-X_{\max}, X_{\max}]. \end{aligned} \tag{18b}$$

At the material interfaces $z = 0$ and $z = Z_{\max}$, the field E and its normal derivative E_z are continuous for all $x \in [-X_{\max}, X_{\max}]$:

$$\begin{aligned} &E(0+,x) = E(0-,x), \quad E_z(0+,x) = E_z(0-,x),\\ &E(Z_{\max}+,x) = E(Z_{\max}-,x), \quad E_z(Z_{\max}+,x) = E_z(Z_{\max}-,x). \end{aligned} \tag{18c}$$

We also consider the case of three spatial dimensions, which models the propagation in bulk medium. In order to reduce the computational costs, we assume that the field is cylindrically symmetric $E(x) \equiv E(z,\rho)$, where $\rho = |x_\perp| = \sqrt{x^2 + y^2}$. This enables us to solve the problem with only two independent spatial variables. In this case, the computational domain in the transverse direction is $\rho \in [0, \rho_{\max}]$, and the scalar NLH equation inside the Kerr medium is

$$\begin{aligned} &E_{zz}(z,\rho) + E_{\rho\rho} + \frac{1}{\rho}E_\rho + k_0^2\left(v^2 + \epsilon|E|^{2\sigma}\right)E = 0,\\ &(z,\rho) \in (0, Z_{\max}) \times [0, \rho_{\max}]. \end{aligned} \tag{19a}$$

The linear Helmholtz outside the Kerr medium is

$$\begin{aligned} &E_{zz}(z,\rho) + E_{\rho\rho} + \frac{1}{\rho}E_\rho + k_0^2 E = 0,\\ &(z,\rho) \in \{[-\delta, 0) \cup (Z_{\max}, Z_{\max} + \delta]\} \times [0, \rho_{\max}] \end{aligned} \tag{19b}$$

and the continuity conditions at the planar interfaces are

$$\begin{aligned} &E(0+,\rho) = E(0-,\rho), \quad E_z(0+,\rho) = E_z(0-,\rho),\\ &E(Z_{\max}+,\rho) = E(Z_{\max}-,\rho), \quad E_z(Z_{\max}+,\rho) = E_z(Z_{\max}-,\rho). \end{aligned} \tag{19c}$$

We shall sometimes find it convenient to adopt a general notation for both cases, by denoting the scalar transverse coordinate as $x_\perp = |x_\perp|$ and its domain by $\Omega_\perp$. In the Cartesian case we have $x_\perp \equiv x$ and $\Omega_\perp = [-X_{\max}, X_{\max}]$, while in the cylindrically symmetric case we have $x_\perp \equiv \rho$ and $\Omega_\perp = [0, \rho_{\max}]$.

We shall also find it convenient to decompose the Laplacian as $\Delta = \partial_{zz} + \Delta_\perp$, where $\Delta_\perp = \partial_{xx}$ in the Cartesian case and $\Delta_\perp = \frac{1}{\rho}\partial_\rho(\rho\partial_\rho) \equiv \partial_\rho^2 + \frac{1}{\rho}\partial_\rho$ in the cylindrically symmetric case. Physically, the transverse Laplacian term $\Delta_\perp E$ leads to diffraction.

Using this notation, the Cartesian system (18a) and the cylindrically symmetric case system (19a) are universally represented as

$$\begin{aligned} &E_{zz}(z,x_\perp) + \Delta_\perp E + k_0^2\left(v^2 + \epsilon|E|^{2\sigma}\right)E = 0,\\ &(z,x_\perp) \in (0, Z_{\max}) \times \Omega_\perp, \end{aligned} \tag{20a}$$

$$\begin{aligned} &E_{zz}(z,x_\perp) + \Delta_\perp E + k_0^2 E = 0,\\ &(z,x_\perp) \in \{[-\delta, 0) \cup (Z_{\max}, Z_{\max} + \delta]\} \times \Omega_\perp, \end{aligned} \tag{20b}$$

$$\begin{aligned} &E(0+,x_\perp) = E(0-,x_\perp), \quad E_z(0+,x_\perp) = E_z(0-,x_\perp),\\ &E(Z_{\max}+,x_\perp) = E(Z_{\max}-,x_\perp), \quad E_z(Z_{\max}+,x_\perp) = E_z(Z_{\max}-,x_\perp). \end{aligned} \tag{20c}$$

3.1.1. Local transverse boundary conditions

Following the approach first used in [20], we set locally one-dimensional radiation boundary conditions of the Sommerfeld type in the transverse direction $x_\perp$. To do so, we assume that the beam is localized around $x_\perp = 0$, so that far from the beam center the nonlinearity becomes negligible, i.e.,

$$\epsilon|E|^{2\sigma} \ll v^2, \quad |x| \geqslant X_{\max} \text{ or } \rho \geqslant \rho_{\max}.$$

Therefore, the field (approximately) satisfies the constant coefficient equation:

$$\Delta E + v_0^2 k_0^2 E = 0, \quad |x| \geqslant X_{\max} \text{ or } \rho \geqslant \rho_{\max}.$$

We further assume that for $|x| \gtrsim X_{\max} (\rho \gtrsim \rho_{\max})$ the field is composed predominantly of the outgoing plane (cylindrical) waves with nearly normal incidence on the boundary $|x| = X_{\max}$ $(\rho = \rho_{\max})$.

This leads to the following radiation boundary conditions in the 2*D* Cartesian case [20]:

$$E_x - ik_0 v_0 E|_{x=X_{max}} = 0, \quad E_z + ik_0 v_0 E|_{x=-X_{max}} = 0. \tag{21a}$$

In the 3*D* cylindrically symmetric case the local radiation boundary condition at $\rho = \rho_{max}$ reads [21]:

$$E_\rho - \alpha E|_{\rho=\rho_{max}} = 0, \quad \alpha = \frac{\frac{d}{d\rho}H_0^{(1)}(v_0 k_0 \rho_{max})}{H_0^{(1)}(v_0 k_0 \rho_{max})}, \tag{21b}$$

where $H_0^{(1)}$ is the Hankel function of the first kind. The symmetry condition at the axis $\rho = 0$ is

$$\frac{\partial}{\partial \rho} E(z,0) = 0. \tag{21c}$$

We emphasize that these transverse boundary conditions are valid as long as the beam is localized around the axis and remains "far" from the transverse boundary at $x = X_{\max}$ or $\rho = \rho_{\max}$.

3.1.2. Nonlocal longitudinal boundary conditions

Similarly to the one-dimensional case (see Section 2.1), the boundary conditions in the longitudinal direction z will be set in the linear regions at $z = -\delta$ and $z = Z_{\max} + \delta$. They should render the boundaries transparent for all the outgoing waves, i.e., eliminate any non-physical reflections, and at the same time correctly prescribe the given incoming wave(s), see Fig. 2. Unlike in the one-dimensional case, however, a two-way Sommerfeld boundary condition of type (8), which is local in the configuration space, cannot be transparent for all the outgoing waves, because these waves travel with different longitudinal velocities that depend on their angle of incidence.

Therefore, to accommodate all angles of incidence, we first separate the variables in the linear Helmholtz equation (20b) by expanding its solution with respect to the eigenfunctions of the transverse Laplacian. These eigenfunctions solve the ordinary differential equation:

$$\Delta_\perp \psi^{(l)}(x_\perp) = -(k_\perp^{(l)})^2 \psi^{(l)} \tag{22}$$

subject to the transverse boundary conditions (21c). The resulting eigenvalue problem is not of the classical Sturm–Liouville type, since its operator is not self-adjoint (because of the radiation boundary conditions). As a result, the eigenfunctions are not orthogonal. Nevertheless, these eigenfunctions are bi-orthogonal [29, Volume I] or, alternatively, real orthogonal, and still form a complete system.

A comprehensive discussion on completeness of eigensystems arising in the diffraction theory, and on convergence of the corresponding series, can be found in [30].

Since the system of eigenfunctions $\{\psi^{(l)}\}$ is complete, we can expand the field E and the incoming beams E^0_{inc} and $E^{Z_{\max}}_{\text{inc}}$ as

$$\begin{aligned} E(z,x_\perp) &= \sum_{l=0}^{\infty} u_l(z)\psi^{(l)}(x_\perp), \\ E^0_{\text{inc}}(x_\perp) &= \sum_{l=0}^{\infty} u^0_{\text{inc},l}\psi^{(l)}(x_\perp), \quad E^{Z_{\max}}_{\text{inc}}(x_\perp) = \sum_{l=0}^{\infty} u^{Z_{\max}}_{\text{inc},l}\psi^{(l)}(x_\perp). \end{aligned} \tag{23}$$

In the transformed space, the linear Helmholtz equation (20b) reduces to a system of uncoupled one-dimensional linear Helmholtz equations (ODEs):

$$\left(\frac{d^2}{dz^2} + (k_\parallel^{(l)})^2\right) u_l(z) = 0, \quad (k_\parallel^{(l)})^2 = k_0^2 - (k_\perp^{(l)})^2, \quad l = 0,1,\ldots,\infty. \tag{24}$$

Each of the uncoupled equations (24) formally coincides with Eq. (6b) and has the same general solution composed of two waves one of which can be interpreted as propagation in the positive z direction and the other one – in the negative z direction. Unlike in Eq. (6b), however, the quantity $(k_\parallel^{(l)})^2$ in Eq. (24) may have a negative real part, in which case the waves become evanescent. It may also have a non-trivial imaginary part, which is due to the non-self-adjoint transverse (radiation) boundary conditions (see [20] for more detail). Regardless of the particular shape that the waves may assume, the longitudinal boundary conditions have to ensure that the field in the region $z \leqslant -\delta$ be of the form [cf. formula (7)]:

$$u(z) = u^0_{\text{inc},l} e^{ik_\parallel^{(l)} z} + C_1 e^{-ik_\parallel^{(l)} z}.$$

Therefore, the two-way ABC at $z = -\delta$ can be written as

$$\left(\frac{d}{dz} + ik_\parallel^{(l)}\right) u_l \Big|_{z=-\delta} = 2ik_\parallel^{(l)} e^{-ik_\parallel^{(l)}\delta} u^0_{\text{inc},l}. \tag{25a}$$

Similarly, at the opposite boundary, $z = Z_{\max} + \delta$, we obtain:

$$\left(\frac{d}{dz} - ik_\parallel^{(l)}\right) u_l \Big|_{z=Z_{\max}+\delta} = -2ik_\parallel^{(l)} e^{-ik_\parallel^{(l)}\delta} u^{Z_{\max}}_{\text{inc},l}. \tag{25b}$$

Boundary conditions (25b) are local in the transformed space $\{u_l(z)\}_{l=0}^{\infty}$. In this space, the two-way one-dimensional Sommerfeld conditions are applied independently for each individual mode defined by (24). The equivalent of relations (25b) after the inverse transformation of (23) will result in a nonlocal pseudodifferential operator in the original space $\{E(z,x)\}$, see [20] or [31] for more details. *Therefore, the resulting boundary conditions are nonlocal two-way artificial BCs.*

3.2. Discrete approximation

We build a semi-compact scheme for the Cartesian problem (18a), (21a), (25b) in Section 3.2.1, and for the cylindrically symmetric problem (19a), (21b), (21c), (25b) in Section 3.2.2. As in the one-dimensional case, we discretize the governing

equations inside and outside the Kerr material, and then obtain a discretization at the material interfaces. The discrete transverse boundary conditions and the discrete two-way ABCs for both problems are described in Section 3.3 and Section 3.4, respectively.

3.2.1. 2D cartesian case

On the rectangle $[-3h_z, Z_{\max}+3h_z]\times[-X_{\max}, X_{\max}]$, we introduce a uniform Cartesian grid of $(N+7)\times M$ nodes as

$$\begin{aligned} &z_n = n\cdot h_z, \quad h_z = \frac{Z_{\max}}{N}, \quad n=-3,-2,\ldots,N+2,N+3,\\ &x_m = -X_{\max} + (m+1/2)h_x, \quad h_x = \frac{2X_{\max}}{M}, \quad m=0,1,\ldots,M-1, \end{aligned} \tag{26}$$

so that

$$z_0 = 0, \quad z_N = Z_{\max}, \quad x_{-1/2} = -X_{\max}, \quad x_{M-1/2} = X_{\max}.$$

In this paper, we keep $h_z \sim h_x$ so that all $\mathcal{O}(h_z^j h_x^{k-j})$ terms can be treated as terms of the same order k and denoted by $\mathcal{O}\left(h^k\right)$. For convenience, we also introduce the following notations for the field and the Kerr nonlinearity at the grid nodes:

$$E_{n,m} \stackrel{\text{def}}{=} E(z_n, x_m), \quad P_{n,m} \stackrel{\text{def}}{=} |E_{n,m}|^{2\sigma} E_{n,m}.$$

Finally, we use the previous notation D for central difference operators, with the order of accuracy in the superscript and the differentiation variables in the subscript.

For example,

$$D^{(2)}_{xx}E \stackrel{\text{def}}{=} \frac{E_{n,m+1} - 2E_{n,m} + E_{n,m-1}}{h_x^2} = \partial_{xx}E_{n,m} + \mathcal{O}\left(h^2\right).$$

Other notations for central differences are listed in Appendix B.

To build a semi-compact approximation of the NLH (18a) at the interior points $n = 1,\ldots,N-1$, we first introduce the following mixed order discrete Laplacian:

$$\begin{aligned} D^{(2)}_{zz}E_{n,m} + D^{(4)}_{xx}E_{n,m} &= \frac{E_{n-1,m} - 2E_{n,m} + E_{n+1,m}}{h_z^2} + \frac{-E_{n,m-2} + 16E_{n,m-1} - 30E_{n,m} + 16E_{n,m+1} - E_{n,m+2}}{12h_x^2}\\ &= \Delta E_{n,m} + \frac{h_z^2}{12}\partial_{zzzz}E_{n,m} + \mathcal{O}\left(h^4\right). \end{aligned} \tag{27}$$

In order to remove the $\mathcal{O}\left(h^2\right)$ term on the right-hand side of (27), we consider the following expression that contains fourth-order derivatives with respect to both z and x, and approximate it to second-order accuracy using central differences:

$$(\partial_{zzzz} - \partial_{xxxx})E_{n,m} = (\partial_{zz} - \partial_{xx})\Delta E_{n,m} = \left(D^{(2)}_{zz} - D^{(2)}_{xx}\right)\Delta E_{n,m} + \mathcal{O}\left(h^2\right). \tag{28}$$

Then, we employ the NLH (18a) itself and substitute the expression

$$\Delta E_{n,m} = -k_0^2\left(v^2 E_{n,m} + \epsilon P_{n,m}\right)$$

into formula (28). Next, we approximate the derivative $\partial_{xxxx}E$ in formula (28) to second-order accuracy using central differences, and altogether obtain:

$$\partial_{zzzz}E_{n,m} = -k_0^2\left(D^{(2)}_{zz} - D^{(2)}_{xx}\right)\left(v^2 E_{n,m} + \epsilon P_{n,m}\right) + D^{(2)}_{xxxx}E_{n,m} + \mathcal{O}\left(h^2\right). \tag{29}$$

Substitution of (29) into (27) yields a semi-compact fourth-order discretization of the Laplacian, which leads to the following fourth-order scheme for the NLH (18a):

$$\begin{aligned} &\left(D^{(2)}_{zz} + D^{(4)}_{xx}E_{n,m} - \frac{h_z^2}{12}D^{(2)}_{xxxx}\right)E_{n,m} + k_0^2\left(1 + \frac{h_z^2}{12}D^{(2)}_{zz} - \frac{h_z^2}{12}D^{(2)}_{xx}\right)\left(v^2 E_{n,m} + \epsilon P_{n,m}\right) = 0, \quad n = 1,\ldots,N-1,\ m\\ &= 0,\ldots,M-1. \end{aligned} \tag{30}$$

To obtain a similar fourth-order scheme for the linear Helmholtz equation (18b), we repeat the previous derivation with $\epsilon P_{n,m} = 0$ and $v = 1$, which yields:

$$\begin{aligned} &\left[\left(1 + \frac{k_0^2 h_z^2}{12}\right)D^{(2)}_{zz} + \left(D^{(4)}_{xx} - \frac{k_0^2 h_z^2}{12}D^{(2)}_{xx} - \frac{h_z^2}{12}D^{(2)}_{xxxx}\right) + k_0^2\right]E_{n,m} = 0, \quad n = -3,\ldots,-1,N+1,\ldots,3,\ m\\ &= 0,\ldots,M-1. \end{aligned} \tag{31}$$

Next, we consider material interfaces at the nodes $n = 0$ and $n = N$. Using Taylor's expansion, we can write:

$$\frac{-85E_{0,m} + 108E_{1,m} - 27E_{2,m} + 4E_{3,m}}{66h_z} = \partial_z E_{0+,m} + \frac{3h_z}{11}\partial_{zz}E_{0+,m} + \mathcal{O}\left(h^4\right).$$

Then, approximating the derivative $\partial_{zz}E_{0+,m}$ with fourth-order accuracy:

$$\partial_{zz}E_{0+,m} = \Delta E_{0+,m} - \partial_{xx}E_{0+,m} = -k_0^2(v_{0+}^2 E_{0,m} + \epsilon_{0+}P_{0,m}) - D_{xx}^{(4)}E_{0,m} + \mathcal{O}\left(h^4\right),$$

we obtain:

$$\partial_z E_{0+,m} = \frac{-85E_{0,m} + 108E_{1,m} - 27E_{2,m} + 4E_{3,m}}{66h_z} + \frac{3h_z k_0^2}{11}\left(v_{0+}^2 E_{0,m} + \epsilon_{0+}P_{0,m}\right) + \frac{3h_z}{11}D_{xx}^{(4)}E_{0,m} + \mathcal{O}\left(h^4\right). \tag{32}$$

Deriving a similar formula for $\partial_z E_{0-,m}$ and equating the resulting expressions for $\partial_z E_{0+,m}$ and $\partial_z E_{0-,m}$, we get a fourth-order accurate approximation of the continuity condition $E_z(0-) = E_z(0+)$:

$$\frac{4E_{-3,m} - 27E_{-2,m} + 108E_{-1,m} - 170E_{0,m} + 108E_{1,m} - 27E_{2,m} + 4E_{3,m}}{66h_z} + \frac{6h_z k_0^2}{11}\left(\frac{v_{0-}^2 + v_{0+}^2}{2}E_{0,m} + \frac{\epsilon_{0-} + \epsilon_{0+}}{2}P_{0,m}\right) + \frac{6h_z}{11}D_{xx}^{(4)}E_{0,m} = 0. \tag{33}$$

Finally, substituting $v_{0-,m} = 1, \epsilon_{0-,m} = 0, v_{0+,m} = v$ and $\epsilon_{0+,m} = \epsilon$, we have:

$$\frac{4E_{-3,m} - 27E_{-2,m} + 108E_{-1,m} - 170E_{0,m} + 108E_{1,m} - 27E_{2,m} + 4E_{3,m}}{66h_z} + \frac{6h_z k_0^2}{11}\left(\frac{1+v^2}{2}E_{0,m} + \frac{\epsilon}{2}P_{0,m}\right) + \frac{6h_z}{11}D_{xx}^{(4)}E_{0,m} = 0. \tag{33a}$$

A similar equation is obtained for the interface at $n = N$:

$$\frac{4E_{N-3,m} - 27E_{N-2,m} + 108E_{N-1,m} - 170E_{N,m} + 108E_{N+1,m} - 27E_{N+2,m} + 4E_{N+3,m}}{66h_z} + \frac{6h_z k_0^2}{11}\left(\frac{1+v^2}{2}E_{N,m} + \frac{\epsilon}{2}P_{N,m}\right) + \frac{6h_z}{11}D_{xx}^{(4)}E_{N,m} = 0. \tag{33b}$$

3.2.2. Cylindrically symmetric case

We use the same grid (26), except that in the transverse direction we now have:

$$\rho_m = (m + 1/2)h_\rho, \quad h_\rho = \frac{\rho_{\max}}{M}, \quad m = 0, \ldots, M-1, \tag{34}$$

so that

$$\rho_{-1/2} = 0 \quad \text{and} \quad \rho_{M-1/2} = \rho_{\max}.$$

We also keep $h_z \sim h_\rho$ so that all $\mathcal{O}(h_z^j h_\rho^{k-j})$ terms appear of the same order $\mathcal{O}\left(h^k\right)$.

To approximate the NLH (19a) at the interior points $n = 1, \ldots, N-1$, we begin by introducing a mixed order discretization of the cylindrical Laplacian $\Delta = \partial_{zz} + \Delta_\rho \equiv \partial_{zz} + \partial_\rho^2 + \frac{1}{\rho}\partial_\rho$:

$$\left(D_{zz}^{(2)} + D_{\rho\rho}^{(4)} + \frac{1}{\rho_m}D_\rho^{(4)}\right)E_{n,m} = \Delta E_{n,m} + \frac{h_z^2}{12}\partial_{zzzz}E_{n,m} + \mathcal{O}\left(h^4\right). \tag{35}$$

To remove the $\mathcal{O}\left(h^2\right)$ term on the right-hand side of (35), we start with the second-order central difference approximation of the expression $(\partial_{zzzz} - \Delta_\rho^2)E_{n,m} = (\partial_{zz} - \Delta_\rho)\Delta E_{n,m}$, where $\Delta_\rho^2 = \rho^{-3}\partial_\rho - \rho^{-2}\partial_{\rho\rho} + 2\rho^{-1}\partial_{\rho\rho\rho} + \partial_{\rho\rho\rho\rho}$, and using the NLH (19a) itself, obtain:

$$\partial_{zzzz}E_{n,m} = -k_0^2\left(D_{zz}^{(2)} - D_{\rho\rho}^{(2)} - \frac{1}{\rho_m}D_\rho^{(2)}\right)\left(v^2 E_{n,m} + \epsilon P_{n,m}\right) + \left(\rho_m^{-3}D_\rho^{(2)} - \rho_m^{-2}D_{\rho\rho}^{(2)} + 2\rho_m^{-1}D_{\rho\rho\rho}^{(2)} + D_{\rho\rho\rho\rho}^{(2)}\right)E_{n,m} + \mathcal{O}\left(h^2\right). \tag{36}$$

Substitution of (36) into (35) yields a semi-compact fourth-order discretization of the cylindrical Laplacian, which leads to the following fourth-order scheme for the NLH (19a):

$$\left(D_{zz}^{(2)} + D_{\rho\rho}^{(4)} + \frac{1}{\rho_m}D_\rho^{(4)}\right)E_{n,m} - \frac{h_z^2}{12}\left(\rho_m^{-3}D_\rho^{(2)} - \rho_m^{-2}D_{\rho\rho}^{(2)} + 2\rho_m^{-1}D_{\rho\rho\rho}^{(2)} + D_{\rho\rho\rho\rho}^{(2)}\right)E_{n,m} + k_0^2\left[1 + \frac{h_z^2}{12}\left(D_{zz}^{(2)} - D_{\rho\rho}^{(2)} - \frac{1}{\rho_m}D_\rho^{(2)}\right)\right]\left(v^2 E_{n,m} + \epsilon P_{n,m}\right) = 0, \quad n = 1, \ldots, N-1, \ m = 0, \ldots, M-1. \tag{37}$$

To obtain a similar fourth-order scheme for the linear Helmholtz equation (19b), we repeat the previous derivation with $\epsilon \equiv 0$ and $v \equiv 1$, which yields:

$$\left(D_{zz}^{(2)} + D_{\rho\rho}^{(4)} + \frac{1}{\rho_m} D_{\rho}^{(4)}\right) E_{n,m} - \frac{h_z^2}{12}\left(\rho_m^{-3} D_{\rho}^{(2)} - \rho_m^{-2} D_{\rho\rho}^{(2)} + 2\rho_m^{-1} D_{\rho\rho\rho}^{(2)} + D_{\rho\rho\rho\rho}^{(2)}\right) E_{n,m}$$
$$+ k_0^2 \left[1 + \frac{h_z^2}{12}\left(D_{zz}^{(2)} - D_{\rho\rho}^{(2)} - \frac{1}{\rho_m} D_{\rho}^{(2)}\right)\right] E_{n,m} = 0, \quad n = -3, \ldots, -1, N+1, \ldots, 3, \; m = 0, \ldots, M-1. \tag{38}$$

The analysis of material interfaces at $n = 0$ and $n = N$ is very similar to that of Section 3.2.1, and we arrive at the following fourth-order accurate approximation of the continuity condition $E_z(0-) = E_z(0+)$:

$$\frac{4E_{-3,m} - 27E_{-2,m} + 108E_{-1,m} - 170E_{0,m} + 108E_{1,m} - 27E_{2,m} + 4E_{3,m}}{66h_z} + \frac{6h_z k_0^2}{11}\left(\frac{v_{0-}^2 + v_{0+}^2}{2} E_{0,m} + \frac{\epsilon_{0-} + \epsilon_0}{2} P_{0,m}\right)$$
$$+ \frac{6h_z}{11}\left(D_{\rho\rho}^{(4)} + \frac{1}{\rho_m} D_{\rho}^{(4)}\right) E_{0,m} = 0. \tag{39}$$

Substituting $v_{0-,m} = 1, \epsilon_{0-,m} = 0, v_{0+,m} = v$ and $\epsilon_{0+,m} = \epsilon$ into (39), we have:

$$\frac{4E_{-3,m} - 27E_{-2,m} + 108E_{-1,m} - 170E_{0,m} + 108E_{1,m} - 27E_{2,m} + 4E_{3,m}}{66h_z} + \frac{6h_z k_0^2}{11}\left(\frac{1+v^2}{2} E_{0,m} + \frac{\epsilon}{2} P_{0,m}\right)$$
$$+ \frac{6h_z}{11}\left(D_{\rho\rho}^{(4)} + \frac{1}{\rho_m} D_{\rho}^{(4)}\right) E_{0,m} = 0. \tag{40a}$$

A similar equation is obtained for the interface at $n = N$:

$$\frac{4E_{N-3,m} - 27E_{N-2,m} + 108E_{N-1,m} - 170E_{N,m} + 108E_{N+1,m} - 27E_{N+2,m} + 4E_{N+3,m}}{66h_z} + \frac{6h_z k_0^2}{11}\left(\frac{1+v^2}{2} E_{N,m} + \frac{\epsilon}{2} P_{N,m}\right)$$
$$+ \frac{6h_z}{11}\left(D_{\rho\rho}^{(4)} + \frac{1}{\rho_m} D_{\rho}^{(4)}\right) E_{N,m} = 0. \tag{40b}$$

3.3. Local transverse boundary conditions

In this section, we briefly describe a discrete approximation of the transverse boundary conditions (21c). In doing so, we follow the approach of [21], where additional details can be found.

Let us first consider the radiation boundary conditions (21a) and (21b) at the "upper" boundary $m = M - 1/2$. We will use their discrete counterparts to express the values of the field at the ghost nodes $E_{n,M}$ and $E_{n,M+1}$ via the values at the inner nodes $E_{n,M-3}, E_{n,M-2}$, and $E_{n,M-1}$, and thus eliminate the ghost nodes. A fourth-order approximation of either Cartesian or cylindrical radiation boundary condition centered around $m = M - 1/2$ (which corresponds to $x = X_{\max}$ or $\rho = \rho_{\max}$) is given by

$$\frac{E_{n,M-2} - 27E_{n,M-1} + 27E_{n,M} - E_{n,M+1}}{24h_\perp} - \alpha \frac{-E_{n,M-2} + 9E_{n,M-1} + 9E_{n,M} - E_{n,M+1}}{16} = 0,$$

where in the Cartesian case $\alpha = iv_0 k_0$, see formula (21a), and in the cylindrical case α is defined in (21b), see [21]. Equivalently, we can write:

$$[c_{-2}, \ldots, c_1] \cdot \begin{bmatrix} E_{n,M-2} \\ \vdots \\ E_{n,M+1} \end{bmatrix} = 0,$$

where

$$[c_{-2}, \ldots, c_1] = [1, -27, 27, -1] - \frac{2\alpha h_\perp}{3}[-1, 9, 9, -1].$$

However, specifying this boundary condition alone is not sufficient, because the fourth-order finite difference equation that we use in the $x_\perp$ direction requires an additional boundary condition. The choice of the latter allows for more flexibility as long as the resulting method is fourth-order accurate and stable.[6] Hereafter, we choose this second condition as the fourth-order accurate extrapolation of the ghost value $E_{n,M+1}$ via $\{E_{n,M-3}, \ldots, E_{n,M}\}$, which can be conveniently written as

$$E_{n,M+1} = \sum_{j=-3}^{0} (-1)^j \binom{4}{1-j} E_{n,M+j}.$$

[6] Stability of these approximations can be studied by the methodology of [32].

Combining the two discrete boundary conditions as

$$\begin{bmatrix} 0, & c_{-2}, & c_{-1}, & c_0, & c_1 \\ -1 & 4 & -6 & 4 & -1 \end{bmatrix} \begin{bmatrix} E_{n,M-3} \\ \vdots \\ E_{n,M+1} \end{bmatrix} = \begin{bmatrix} 0 \\ 0 \end{bmatrix},$$

we can express the ghost values $E_{n,M}$ and $E_{n,M+1}$ in terms of the interior values:

$$\begin{bmatrix} E_{n,M} \\ E_{n,M+1} \end{bmatrix} = -\frac{1}{c_0 + 4c_1} \begin{bmatrix} -c_1 & c_{-2} + 4c_1 & c_{-1} - 6c_1 \\ c_0 & 4c_{-2} - 4c_0 & 4c_{-1} + 6c_0 \end{bmatrix} \cdot \begin{bmatrix} E_{n,M-3} \\ E_{n,M-2} \\ E_{n,M-1} \end{bmatrix}. \tag{41a}$$

In the Cartesian case, the derivation is repeated to obtain the discrete discrete radiation boundary condition at $x = -X_{\max}$, i.e., at $m = 0$:

$$\begin{bmatrix} E_{n,-2} \\ E_{n,-1} \end{bmatrix} = -\frac{1}{c_0 + 4c_1} \begin{bmatrix} 4c_{-1} + 6c_0 & 4c_{-2} - 4c_0 & c_0 \\ c_{-1} - 6c_1 & c_{-2} + 4c_1 & -c_1 \end{bmatrix} \cdot \begin{bmatrix} E_{n,0} \\ E_{n,1} \\ E_{n,2} \end{bmatrix}. \tag{41b}$$

In the cylindrical case, the symmetry (21c) is enforced as follows:

$$E_{n,-1} = E_{n,0}, \quad E_{n,-2} = E_{n,1}. \tag{42}$$

Note also that in the Cartesian case there is an alternative way of building the discrete transverse boundary conditions. It does not require a finite difference approximation of the continuous boundary conditions (21a), and is rather based on analyzing the roots of the fourth-order characteristic equation that corresponds to the five node discretization in the x direction. The idea is similar to that behind boundary conditions (17a), and the reader is referred to [20] for more detail.

3.4. Nonlocal longitudinal boundary conditions

In this section, we construct a discrete counterpart for the two-way ABCs (25b). In the continuous case of Section 3.1, we separated the variables in the linear Helmholtz equation (20b) outside the Kerr region, and then obtained the ABCs in the transformed space. In the discrete case, we also begin by separating the variables in the Cartesian (31) and cylindrical (38) difference Helmholtz equation at the exterior grid nodes:

$$m = 0, \ldots, M-1, \quad n = 0, -1, -2, \quad n = N,\ N+1,\ N+2.$$

Subsequently, we derive the ABCs in the transformed space. This derivation is identical for the Cartesian geometry of Section 3.2.1 and the cylindrical geometry of Section 3.2.2.

We first identify the transverse components in the finite difference operators of (31) and (38). The transverse part of the discrete Laplacian for the Cartesian case is

$$L^{\perp} = D^{(4)}_{xx} - \frac{k_0^2 h_z^2}{12} D^{(2)}_{xx} - \frac{h_z^2}{12} D^{(2)}_{xxxx}, \tag{43a}$$

whereas for the cylindrically symmetric case it is given by

$$L^{\perp} = D^{(4)}_{\rho\rho} + \frac{1}{\rho_m} D^{(4)}_{\rho} - \frac{k_0^2 h_z^2}{12} \left(D^{(2)}_{\rho\rho} + \frac{1}{\rho_m} D^{(2)}_{\rho} \right) - \frac{k_0^2 h_z^2}{12} \left(\rho_m^{-3} D^{(2)}_{\rho} - \rho_m^{-2} D^{(2)}_{\rho\rho} + 2\rho_m^{-1} D^{(2)}_{\rho\rho\rho} + D^{(2)}_{\rho\rho\rho\rho} \right). \tag{43b}$$

The separation of variables in Eqs. (31) and (38) will be rendered by expanding the solution with respect to the transverse eigenvectors $\psi^{(l)} = [\psi_0^{(l)}, \psi_1^{(l)}, \ldots, \psi_{M-1}^{(l)}]^T$. Each eigenvector $\psi^{(l)}$ satisfies the following difference equation on the grid (cf. Eq. (22)):

$$L^{\perp} \psi_m^{(l)} = -(k_{\perp}^{(l)})^2 \psi_m^{(l)}, \quad m = 0, 1, \ldots, M-1. \tag{44}$$

In the Cartesian case, the operator $L^{\perp}$ in (44) is defined by formula (43a), and the solution $\psi^{(l)}$ is subject to boundary conditions (41a) and (41b). In the cylindrically symmetric case, the operator $L^{\perp}$ in (44) is defined by formula (43b), and the solution $\psi^{(l)}$ is subject to boundary conditions (41a) and (42). The argument behind linear independence of $\{\psi^{(l)}\}$ in the Cartesian case is based on bi-orthogonality (real orthogonality) of the eigenvectors and can be found in [20]. For the cylindrically symmetric case, the continuous eigenfunctions are also real orthogonal, but the discrete eigenvectors are not, see [21]. Yet we observe numerically that they are linearly independent.

The M linearly independent eigenvectors are convenient to arrange as a column matrix:

$$\Psi \stackrel{\text{def}}{=} \left[\psi^{(0)}, \psi^{(1)}, \ldots, \psi^{(M-1)} \right] = \begin{bmatrix} \psi_0^{(0)} & \cdots & \psi_0^{(M-1)} \\ \vdots & \ddots & \vdots \\ \psi_{M-1}^{(0)} & \cdots & \psi_{M-1}^{(M-1)} \end{bmatrix},$$

that will diagonalize the discrete transverse Laplacian, i.e., $L^{\perp}\Psi = \Psi\Lambda$, where

$$\Lambda = \operatorname{diag}\left\{-(k_{\perp}^{(0)})^2, -(k_{\perp}^{(1)})^2, \ldots, -(k_{\perp}^{(M-1)})^2\right\}$$

and the eigenvalues $-(k_{\perp}^{(l)})^2$ are defined in (44).

It will also be convenient to consider the following M-dimensional vectors:

$$\mathscr{E}_n \stackrel{\text{def}}{=} [E_{n,0}, E_{n,1}, \ldots, E_{n,M-1}]^T,$$

that contain the values of the field arranged in the transverse direction. With this notation, we can recast both scheme (31) and scheme (38) in the vector form:

$$\left(1 + \frac{k_0^2 h_z^2}{12}\right)\frac{\mathscr{E}_{n+1} - 2\mathscr{E}_n + \mathscr{E}_{n-1}}{h_z^2} + L^{\perp}\mathscr{E}_n + k_0^2\mathscr{E}_n = 0. \tag{45}$$

For each n, let us introduce the vector variable

$$U_n = \Psi^{-1}\mathscr{E}_n. \tag{46a}$$

Equality $\mathscr{E}_n = \Psi U_n$ is the expansion of $\mathscr{E}_n$ with respect to the eigenvectors $\psi^{(l)}$, where the coefficients are given by the components of U_n. Similarly, we can expand the incoming beam profiles:

$$U_{\text{inc}}^0 = \Psi^{-1}\mathscr{E}_{\text{inc}}^0, \quad U_{\text{inc}}^0 \stackrel{\text{def}}{=} \begin{bmatrix} u_{\text{inc},0}^0 \\ \vdots \\ u_{\text{inc},M-1}^0 \end{bmatrix}, \quad \mathscr{E}_{\text{inc}}^0 \stackrel{\text{def}}{=} \begin{bmatrix} E_{\text{inc},0}^0 \\ \vdots \\ E_{\text{inc},M-1}^0 \end{bmatrix}, \tag{46b}$$

$$U_{\text{inc}}^{\text{Zmax}} = \Psi^{-1}\mathscr{E}_{\text{inc}}^{\text{Zmax}}, \quad U_{\text{inc}}^{\text{Zmax}} \stackrel{\text{def}}{=} \begin{bmatrix} u_{\text{inc},0}^{\text{Zmax}} \\ \vdots \\ u_{\text{inc},M-1}^{\text{Zmax}} \end{bmatrix}, \quad \mathscr{E}_{\text{inc}}^{\text{Zmax}} \stackrel{\text{def}}{=} \begin{bmatrix} E_{\text{inc},0}^{\text{Zmax}} \\ \vdots \\ E_{\text{inc},M-1}^{\text{Zmax}} \end{bmatrix}. \tag{46c}$$

Formulae (46a) are discrete counterparts of (23). Substituting expansions (46a) into Eq. (45) and diagonalizing $L^{\perp}$: $L^{\perp}\mathscr{E}_n = L^{\perp}\Psi U_n = \Psi\Lambda U_n$, we have:

$$\Psi\left(1 + \frac{k_0^2 h_z^2}{12}\right)\frac{U_{n+1} - 2U_n + U_{n-1}}{h_z^2} + \Psi\Lambda U_n + \Psi k_0^2 U_n = 0. \tag{47}$$

Finally, multiplying Eq. (47) by the inverse matrix Ψ^{-1} from the left we separate the variables. Recasting the result via individual components of $U_n = [u_{n,0}, u_{n,1}, \ldots, u_{n,M-1}]^T$, we obtain:

$$\left(1 + \frac{k_0^2 h_z^2}{12}\right)\frac{u_{n+1,l} - 2u_{n,l} + u_{n-1,l}}{h_z^2} - (k_{\perp}^{(l)})^2 u_{n,l} + k_0^2 u_{n,l} = 0, \quad l = 0, 1, \ldots, M-1. \tag{48}$$

Formula (48) is a system of M uncoupled ordinary difference equations, which is a discrete counterpart of the continuous uncoupled system (24).

Each of the uncoupled difference equation (48) is identical to the one-dimensional difference equation (15) if we redefine k^2 of (15) as

$$k^2 = \frac{k_0^2 - (k_{\perp}^{(l)})^2}{1 + \frac{k_0^2 h_z^2}{12}} \equiv \frac{(k_{\parallel}^{(l)})^2}{1 + \frac{k_0^2 h_z^2}{12}}.$$

Therefore, similarly to (17a) we can write for the ghost node $n = -4$:

$$u_{-4,l} = (q_l^{-1} - q_l)q_l^{-3}u_{\text{inc},l}^0 + q_l u_{-3,l},$$

where q_l and q_l^{-1} denote roots of the characteristic equation for a given l, and the incoming components $u_{\text{inc},l}^0$ are defined in (46a).

Recasting the previous equality in the matrix form and transforming back into the configuration space, $\mathscr{E} = \Psi U$, we obtain the two-way discrete ABCs:

$$\mathscr{E}_{-4} = \Psi\begin{bmatrix} \frac{q_0^{-1} - q_0}{q_0^3} & & \\ & \ddots & \\ & & \frac{q_{M-1}^{-1} - q_{M-1}}{q_{M-1}^3} \end{bmatrix}\Psi^{-1}\mathscr{E}_{\text{inc}}^0 + \Psi\begin{bmatrix} q_0 & & \\ & \ddots & \\ & & q_{M-1} \end{bmatrix}\Psi^{-1}\mathscr{E}_{-3}. \tag{49a}$$

Likewise, for the ghost node $n = N + 4$ we write similarly to (17b):

$$u_{N+4,l} = \left(q_l^{-1} - q_l\right) q_l^{-3} u_{\mathrm{inc},l}^{Z\max} + q_l u_{N+3,l},$$

and arrive at the following two-way discrete ABCs:

$$\mathscr{E}_{N+4} = \Psi \begin{bmatrix} \frac{q_0^{-1}-q_0}{q_0^3} & & \\ & \ddots & \\ & & \frac{q_{M-1}^{-1}-q_{M-1}}{q_{M-1}^3} \end{bmatrix} \Psi^{-1} \mathscr{E}_{\mathrm{inc}}^{\mathrm{Zmax}} + \Psi \begin{bmatrix} q_0 & & \\ & \ddots & \\ & & q_{M-1} \end{bmatrix} \Psi^{-1} \mathscr{E}_{N+3}. \tag{49b}$$

Relations (49a) provide a fourth-order accurate approximation to the boundary conditions (25b) for $\delta = 3h_z$. In the Cartesian or cylindrical case, relation (49a) is substituted into Eq. (31) or (38), respectively, for $n = -3$, and relation (49b) is substituted into Eq. (31) or (38), respectively, for $n = N + 3$. This eliminates the ghost values from the schemes (31) and (38) and thus closes the system of finite-difference equations on the grids (26) and (34).

3.5. Extension to the multi-layer material

In the case of a grated Kerr material described in Section 1.3, there are additional discontinuity points defined by formula (5a). The interface conditions at each discontinuity point $\tilde{z}$ are the same as at $z = 0$ and $z = Z_{\max}$:

$$E(\tilde{z}+, x_\perp) = E(\tilde{z}-, x_\perp), \quad \frac{\partial E}{\partial z}(\tilde{z}+, x_\perp) = \frac{\partial E}{\partial z}(\tilde{z}-, x_\perp).$$

In the simple case when $\tilde{z}$ coincides with one of the grid nodes, the discrete approximation of the continuity conditions is given by the same formula as (33) for the Cartesian case and by the same formula as (39) for the cylindrical case. Hence, to solve the one-dimensional NLH for the multi-layer case one needs to apply the corresponding discrete interface condition of type (33) or (39) at each plane (5a). The extension to the case when a discontinuity plane does not coincide with any of the uniform grid surfaces (26) or (34) can be obtained by building separate grids for different layers.

4. Newton's solver

Here we briefly outline our approach to building a Newton type solver for the NLH. The reader is referred to [19, Section 3] for a detailed description.

The schemes for the NLH that we constructed in Sections 2 and 3 lead to systems of nonlinear difference equations that we symbolically write as

$$F(E) = 0,$$

where the quantities F and E are complex. In the one-dimensional case, they are vectors of dimension $N + 7$, which is the dimension of grid (9), $F, E \in \mathbb{C}^{N+7}$. In the two-dimensional case, F and E can be interpreted as matrices of dimension $(N + 7) \times M$, which is the dimension of grid (26), and for convenience we reshape them as $(N + 7)M$-dimensional vectors: $F, E \in \mathbb{C}^{(N+7)M}$.

To linearize the transformation $F(E)$, we first notice that the Kerr nonlinearity $P = |E|^{2\sigma}E$ is Frechét nondifferentiable as long as E is complex. To overcome this, we separate the real and imaginary parts and recast the field E and mapping F as real vectors of twice the dimension:

$$E \in \mathbb{C}^{(N+7)M} \to \widehat{E} \in \mathbb{R}^{2(N+7)M},$$
$$F(E) : \mathbb{C}^{(N+7)M} \mapsto \mathbb{C}^{(N+7)M} \to \widehat{F}(\widehat{E}) : \mathbb{R}^{2(N+7)M} \mapsto \mathbb{R}^{2(N+7)M}.$$

The new transformation $\widehat{F}(\widehat{E})$ is differentiable in the conventional real sense. Differentiation results in Newton's linearization of $\widehat{F}$ that involves the Jacobian $\widehat{J}$, and leads to Newton's iterations:

$$\widehat{E}^{(j+1)} - \widehat{E}^{(j)} \stackrel{\mathrm{def}}{=} \delta E^{(j+1)} = -\left[\widehat{\widehat{J}}(E^{(j)})\right]^{-1} \widehat{F}(E^{(j)}). \tag{50}$$

The convergence of Newton's method is known to be very sensitive to the choice of the initial guess. In our experiments, we take the simplest initial guess $E^{(0)} \equiv 0$. We have also observed numerically that the algorithm was more likely to converge if, during the first stage of the iteration process, when the iterations $E^{(j)}$ are "far" from the solution, we introduce the relaxation mechanism:

$$\widehat{E}^{(j+1)} - \widehat{E}^{(j)} = \frac{\omega}{\max\left\{1, \|\delta E^{(j+1)}\|_\infty\right\}} \delta E^{(j+1)}, \tag{51}$$

where $\omega \in (0, 1]$; typically $\omega = 0.5$. While this mechanism enables the algorithm to converge for a wider range of cases, it also slows down the convergence (from quadratic to linear rate). Therefore, once the iterates $E^{(j)}$ are "sufficiently close" to the solution so that $\|\delta E^{(j)}\|_\infty < 0.01$, we change back to $\omega = 1$, thereby reverting to the original Newton's method (50).

The criterion for convergence that we employ is the inter-iteration distance threshold $|\delta E^{(j)}| < 10^{-12}$.

5. Summary of the numerical method

The NLH (20c) subject to local transverse boundary conditions (21c) and nonlocal two-way longitudinal boundary conditions (25b) is discretized on the grid (26) or (34). In the Cartesian case, we obtain semi-compact schemes (30) and (31) in the interior and exterior of the Kerr material, respectively, and discretization (33a) for the continuity conditions at the interface. In the cylindrically symmetric case, we arrive at the semi-compact schemes (37) and (38) at the interior and exterior nodes, respectively, and discretization (40a) for the continuity conditions at the interface. For both geometries, we also employ discretization (41a) for the local transverse radiation boundary condition, and discretization (49a) for the non-local two-way boundary conditions at $z = -3h_z$ and $z = Z_{\max} + 3h_z$. In addition, discretization (42) is used at the axis of the cylindrical system.

The resulting system of nonlinear difference equations with respect to complex unknowns $E_{n,m}$ is recast in the real form at the expense of doubling its dimension. Then, Newton's linearization is applied, see formula (50), which yields a $2(N+7)M \times 2(N+7)M$ sparse Jacobian matrix, with the bandwidth of $2M$ for the interior and exterior grid points, where $n \neq 0, N$. For the points at the interfaces, where $n = 0$ or $n = N$, the bandwidth is $6M$.

At each Newton's iteration (50) or (51), this Jacobian needs to be inverted. Currently, we are using a sparse direct solver to invert the Jacobians. This entails an $\mathcal{O}(N \cdot M^2)$ memory cost and hence imposes a fairly strict limit on the grid dimension. For example, a typical grid dimension of $N \times M = 1000 \times 320$ results in the memory requirement of about 6 Gb.

6. Finding an NLS-compatible incoming beam

As indicated in Section 1.1, the NLH is the simplest nonparaxial model that generalizes the NLS. Accordingly, one of our key goals is to investigate how the addition of nonparaxiality affects the solution. In order to do so, we shall use the NLS solutions as "benchmarks," and compare them with NLH solutions computed for "similar" input parameters.

We note that for an incoming beam $E_{\text{inc}}^{0,\text{NLH}}$ which impinges on the material interface at $z = 0-$, only a part of it that we denote by $E_{\text{refracted}}$ passes through whereas the rest gets reflected. In contradistinction to that, in the NLS framework all of the incoming beam $E_{\text{inc}}^{0,\text{NLS}}$ propagates forward.

Therefore, in order to have comparable incoming beams for these two models, we should choose the NLH incoming beam $E_{\text{inc}}^{0,\text{NLH}}$ so that the *refracted* part of it at $z = 0+$ be close to the NLS initial data $E_{\text{inc}}^{0,\text{NLS}}$, i.e.,

$$E_{\text{refracted}}^{\text{NLH}}(0+, x_\perp) \approx E_{\text{inc}}^{0,\text{NLS}}(x_\perp). \tag{52}$$

A comprehensive solution to this problem is nontrivial, because the reflection at the nonlinear interface $z = 0$ depends on the NLH solution itself for $z > 0$. Therefore, in this paper we use an approximate treatment which experimentally proves sufficient.

In order to present this approximate treatment, let us first consider the one-dimensional linear problem:

$$\frac{d^2E(z)}{dz^2} + v^2(z)E = 0, \quad v(z) = \begin{cases} 1, & z < 0, \\ v, & z > 0, \end{cases} \tag{53a}$$

with the wave $E_{\text{inc}}^{0,\text{NLH}} e^{iz}$ impinging on the interface from the left. The overall field has the form:

$$E(z) = \begin{cases} E_{\text{inc}}^{0,\text{NLH}} e^{iz} + Re^{-iz}, & -\infty < z \leqslant 0, \\ Te^{ivz}, & 0 \leqslant z < \infty, \end{cases} \tag{53b}$$

where R and T are the reflection and transmission (refraction) coefficients. The values of R and T are obtained from the continuity condition at the interface

$$E(0-) = E(0+), \quad \frac{dE}{dz}(0-) = \frac{dE}{dz}(0+), \tag{53c}$$

which yields:

$$|E_{\text{refracted}}^{\text{NLH}}(0+)| = |T| = \frac{2}{1+v}|E_{\text{inc}}^{0,\text{NLH}}|. \tag{54}$$

Formula (54) is a standard result for the transmission of plane waves with normal incidence at a single linear interface, see, e.g., [33, Section 7.3, Eq. (7.42)].

We shall use this simple refraction formula to approximate the refracted beam of our weakly nonlinear multi-dimensional problem:

$$E_{\text{refracted}}^{\text{NLH}}(0+, x_\perp) \approx \frac{2}{1 + \sqrt{v^2 + \epsilon|E(0+, x_\perp)|^{2\sigma}}} E_{\text{inc}}^{0,\text{NLH}}(x_\perp).$$

Next, we assume that the NLH solution is close to the refracted incoming beam, $E(0+, x_\perp) \approx E_{\text{refracted}}(0+, x_\perp)$, and obtain:

$$E_{\text{refracted}}^{\text{NLH}}(0+, x_\perp) \approx \frac{2}{1 + \sqrt{v^2 + \epsilon|E_{\text{refracted}}(0+, x_\perp)|^{2\sigma}}} E_{\text{inc}}^{0,\text{NLH}}(x_\perp).$$

Finally, requirement (52) implies:

$$E_{\mathrm{inc}}^{0,\mathrm{NLH}}(x_\perp) = \frac{1+\sqrt{v^2+\epsilon\left|E_{\mathrm{inc}}^{0,\mathrm{NLS}}(x_\perp)\right|^{2\sigma}}}{2} E_{\mathrm{inc}}^{0,\mathrm{NLS}}(x_\perp). \tag{55}$$

Eq. (55) will be used throughout Section 7 for all collimated incoming beams.

7. Numerical experiments

7.1. 2D cubic NLH (solitons)

7.1.1. A single collimated beam (nonparaxial soliton)

The Cartesian configuration ($D = 2$) models propagation in planar waveguides. In the case of a cubic nonlinearity ($\sigma = 1$) and $v = 1$, the one-dimensional NLS (4) has solitary wave solutions:

$$E(z,x) = \left(\frac{2f^2}{\epsilon}\right)^{1/2} \frac{\exp\left(ik_0 z(1+\frac{f^2}{2})\right)}{\cosh(fk_0 x)} = \frac{\sqrt{2}}{k_0 r_0\sqrt{\epsilon}} \frac{\exp\left(ik_0 z(1+\frac{1}{2}(k_0 r_0)^{-2})\right)}{\cosh(x/r_0)} \tag{56}$$

which are called solitons. In formula (56), r_0 is the soliton width and $f = (k_0 r_0)^{-1}$ is the nonparaxiality parameter, which can also be interpreted as the reciprocal beam width measured in linear wavelengths: $2\pi f = \lambda_0/r_0$.

We solve the Cartesian NLH (18a) on an elongated domain: $Z_{\max} = 240, X_{\max} = 12$, and for $k_0 = 2\pi/\lambda_0 = 4, v = 1$, and $\epsilon = k_0^{-2}$.

The problem is driven by the incoming beam

$$E_{\mathrm{inc}}^0(x) = \frac{1+\sqrt{1+\epsilon\,\mathrm{sech}^2\left(x/\sqrt{2}\right)}}{2}\,\mathrm{sech}\left(x/\sqrt{2}\right)$$

for which the refracted beam is (approximately) an NLS soliton profile of the width $r_0 = \sqrt{2}$:

$$E_{\mathrm{refracted}}^0 \approx \mathrm{sech}\left(x/\sqrt{2}\right),$$

see formula (55). The corresponding nonparaxiality parameter is $f = 1/\sqrt{32} \approx 0.177$, which means $r_0 = 0.90\cdot\lambda_0$ and which is considered a very narrow beam.

In this simulation, the field was assumed symmetric with respect to the x-axis, $E(x) = E(-x)$. This allows us to increase the resolution in the x direction by a factor of two. A non-symmetric simulation at half the resolution provides very similar results. The grid dimension that we took was $N \times M = 4480 \times 112$, which translates into the resolution of $\lambda_0/h_z = 30$ and $\lambda_0/h_x = 15$, i.e., 30 grid points per linear wavelength in the z direction (axial) and 15 grid points per linear wavelength in the x direction (transverse).

In Fig. 4(a), we plot the on-axis amplitude of the Cartesian NLH solution. The square amplitude $|E|^2$ exhibits fast oscillations in the z direction, as can be seen in the insert of Fig. 4(a), and in Fig. 4(b). Although at a first glance these oscillations may appear a manifestation of numerical instability, in fact they are physical and indicate the presence of a backward propagating component of the field. Indeed, for a field with both forward and backward propagating components:

$$E \approx Ae^{ik_0 z} + Be^{ik_0 z}, \tag{57}$$

the square amplitude is given by the expression:

$$|E|^2 \approx |A|^2 + 2\mathrm{Re}\left(AB^* e^{2ik_0 z}\right) + |B|^2, \tag{58}$$

which has a $\sim 2k_0$ oscillating term. We note that the amplitude oscillations in Fig. 4(a) and (b) are indeed $\sim 2k_0$, as predicted by formula (58). We further note that these oscillations are also exhibited by the explicit solutions of the 1D NLH [8].

We recall that for the NLS the square amplitude $|A|^2$ is proportional to the energy flux density,[7] and that the L_2 norm of the solution $\|A\|_2^2 = \int |A|^2 dx_\perp$ is a conserved quantity proportional to the total energy flux or, equivalently, the beam power. For the NLH, however, the proper measure of the energy flux density is the Poynting vector:

$$S = k_0^{-1}\mathrm{Im}(E^*\nabla E)$$

rather than the square amplitude. Accordingly, the conserved beam power (i.e., the total energy flux) is the integral its z component over the beam cross-section:

$$N = \int S_z dx_\perp, \quad S_z = k_0^{-1}\mathrm{Im}(E^* E_z).$$

[7] In the Gaussian system, the quantity $\frac{c}{4\pi}|E|^2$ has the units of energy flux: $\frac{\mathrm{erg}}{\mathrm{cm}^2\cdot\mathrm{sec}}$, i.e., of energy per unit area per unit of time.

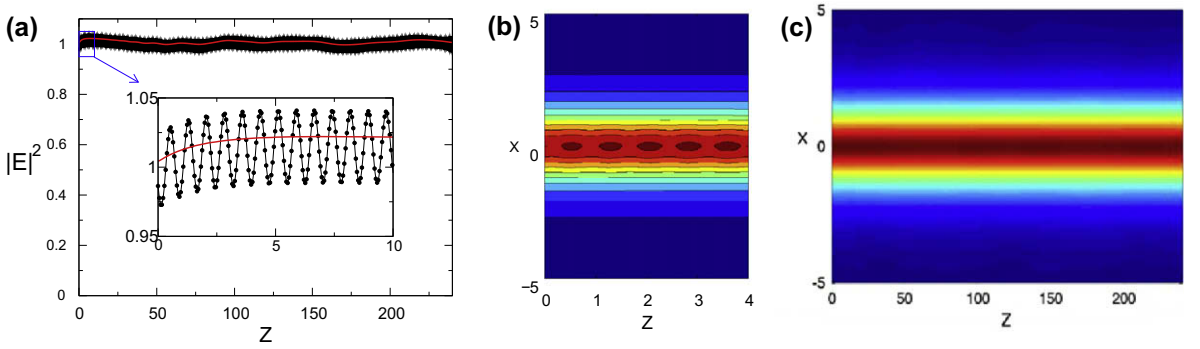

Fig. 4. A nonparaxial soliton for the 2D Cartesian NLH with cubic Kerr nonlinearity. (a) Normalized on-axis $|E|^2$ (black, dotted) and S_z (red). (b) $|E|^2$ contour plot (zoom in on several oscillations). (c) S_z surface plot. (For interpretation of the references to color in this figure legend, the reader is referred to the web version of this article.)

Then, for the field (57) with both forward and backward propagating components, the energy flux density reduces to

$$S_z \approx \left(|A|^2 - |B|^2\right), \tag{59}$$

i.e., to the difference of the forward and backward square amplitudes. Clearly, expression (59) contains no (rapidly) oscillating terms. The Poynting flux S_z for the 2*D* NLH solution is given in Fig. 4(c), and is indeed much smoother than the amplitude, see Fig. 4(a). We therefore suggest that the energy flux density provides a more adequate quantitative measure of the long-scale (collapse) dynamics in the NLH model.

The key physical question that the simulations in this section attempt to answer was whether there exist any solitons beyond the paraxial limit, i.e., of the $\mathcal{O}(\lambda_0)$ radius. Considering the energy flux of the 2*D* NLH solution with $\sigma = 1$ shown in Fig. 4(c), we see that it indeed resembles a soliton propagating essentially unchanged in the positive z direction. We can therefore conclude that such a nonparaxial soliton does exist.

Let us also note that nonparaxial solitons (solutions of the NLH, rather than NLS) for a single collimated beam were obtained in [34] for the case of a semi-infinite Kerr medium. Our formulation is different as it involves a finite-width Kerr material slab with the interfaces that may partially reflect the waves. Hence, a direct comparison of our results with those of [34] is not appropriate. However, a comparison from the standpoint of physics may be of interest for the future.

7.1.2. Grid convergence study

In order to demonstrate the fourth-order grid convergence in the nonlinear regime, we simultaneously refine the grid in the transverse and longitudinal direction, and monitor the maximum difference between the computed fields for each pair of consecutive grids, the coarser and the finer, that differ by a factor of 2 in size. For the grids with fewer than roughly 7 points per linear wavelength, the iterations diverge, apparently due to insufficient resolution. Hence, we choose our coarsest grid to have $\lambda_0/h_z = 7.5$ nodes per wavelength, and compare the results with those on the twice as fine grid, $\lambda_0/h_z = 15$. Then, we keep decreasing the size and hence increasing the dimension of the grid, and the largest dimension that we can take is limited by the memory requirements of the LU solver that we employ for inverting the Jacobians (see Sections 4 and 5). Currently, it is close to $N \times M = 4480 \times 112$, which corresponds to 30 points per linear wavelength in the z direction. The results of the grid convergence study are summarized in Table 1. The convergence rate that we find is $\mathcal{O}(h^{3.8})$, which is close to the design rate of $\mathcal{O}(h^4)$.

7.1.3. Collision of nonparaxial solitons

The NLH is an elliptic equation with no preferred direction of propagation. Therefore, it can be used to model the interaction of beams traveling at different angles, and specifically counter-propagating beams. To demonstrate this capability, we solve the 2*D* NLH with $\sigma = 1$ for two configurations. In the first one, two perpendicular nonparaxial solitons collide, while in the second one, two counter-propagating beams collide almost head-on, at the angle of 150°. Note that the paraxial approximation is invalid in the region of interaction between the beams for either case.

For the perpendicular beam configuration, we solve the 2*D* NLH with $k_0 = 6$, $Z_{\max} = 20, X_{\max} = 30, \nu^2 = 1$, and $\epsilon = k_0^{-2}$. The forward-traveling incoming beam enters the material slab at $z = 0, x = 10$, and propagates in the $-45°$ direction, while

Table 1
Grid convergence study for the 2D Cartesian NLH with $\sigma = 1$, $k_0 = 4, \epsilon = k_0^{-2}, Z_{\max} = 240$, and $X_{\max} = 40$.

(h_z, h_ρ)	$(\frac{\lambda_0}{15}, \frac{\lambda_0}{7.5})$	$(\frac{\lambda_0}{21}, \frac{\lambda_0}{10})$	$(\frac{\lambda_0}{30}, \frac{\lambda_0}{15})$
$\|E^{(2h)} - E^{(h)}\|_\infty$	1.1	0.30	0.080
$\log_2 \|E^{(2h)} - E^{(h)}\|_\infty$	0.20	−1.7	−3.6

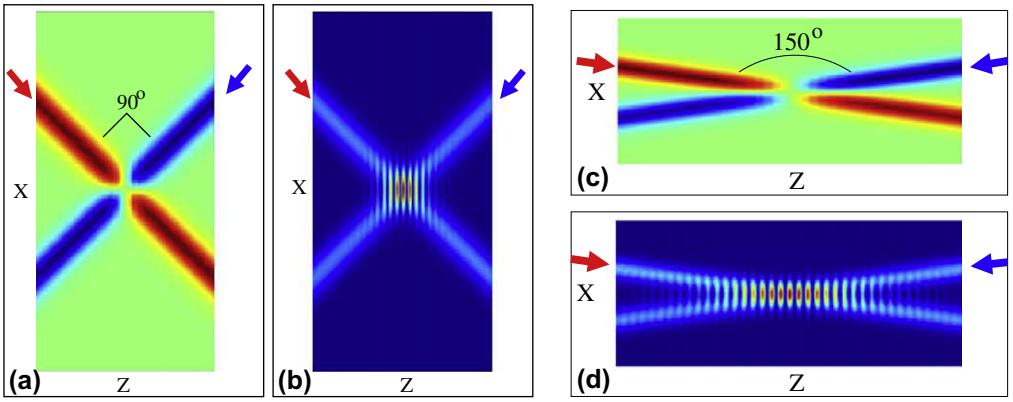

Fig. 5. Collisions of two nonparaxial solitons in the 2D Cartesian NLH with cubic Kerr nonlinearity. (a) Collision angle $90^\circ, S_z$ surface plot. (b) Collision angle $90^\circ, |E|^2$ surface plot. (c) Collision angle $150^\circ, S_z$ surface plot. (d) Collision angle $150^\circ, |E|^2$ surface plot.

its counterpart enters at $z = Z_{\max}, x = 10$, and propagates in the -135° direction. The resolutions were $\lambda_0/h_z = \lambda_0/h_x = 10$ points per linear wavelength. A surface plot of the energy flux density S_z is shown in Fig. 5(a). Positive values of S_z (forward propagation) are red, while negative values (backward propagation) are blue. As in the paraxial NLS model, the two nonparaxial solitons are almost unchanged by the collision. A surface plot of $|E|^2$ is shown in Fig. 5(b); the oscillations in the interaction region are due to the presence of counter-propagation waves.

For the head-on collision configuration, we solve the 2*D* NLH with $k_0 = 4$, $Z_{\max} = 30, X_{\max} = 12$, $v^2 = 1$ and $\epsilon = k_0^{-2}$. The forward-traveling incoming beam enters the material slab at $z = 0, x = 4$, and propagates in the -15° direction, while its counterpart enters at $z = Z_{\max}, x = 4$, and propagates in the -165° direction, resulting in a collision at the angle of 150°. The resolutions were $\lambda_0/h_z = \lambda_0/h_x = 16$ points per linear wavelength. The results presented in Fig. 5(c) and Fig. 5(d) show that as in the previous case, the solitons re-emerge essentially intact after the collision.

7.2. Arrest of collapse in the NLH

7.2.1. 3D cylindrically symmetric case

We solve the cylindrically symmetric NLH (19a) for $\sigma = 1, k_0 = 2\pi/\lambda_0 = 8, v = 1, Z_{\max} = 9$, and $\rho_{\max} = 3.5$. The problem is driven by the incoming beam $E^0_{\text{inc}}(\rho) = \frac{1+\sqrt{1+\epsilon e^{-2\rho^2}}}{2} e^{-\rho^2}$, for which the refracted beam is approximately a Gaussian: $E^0_{\text{refracted}} \approx e^{-\rho^2}$, see formula (55).

The grid dimension is $N \times M = 1080 \times 360$, which translates into the resolution of $\lambda_0/h_z = 94$ and $\lambda_0/h_\rho = 81$, i.e., 94 grid points per linear wavelength in the z direction (axial) and 81 grid points per linear wavelength in the ρ direction (radial).

While this estimate shows that the waves in the linear region are very well resolved, we note that the NLH

$$\Delta E + k_{\text{NL}}^2\left(|E|^2\right)E = 0, \quad k_{\text{NL}}^2 = k_0^2\left(1 + \epsilon|E|^2\right),$$

supports waves with *nonlinear* wavenumber k_{NL}. In order to ensure that these nonlinear waves are also well resolved, a similar resolution estimate should be performed for the *nonlinear* wavelength $\lambda_{\text{NL}} = \lambda_0/\sqrt{1 + \epsilon|E|^2}$. Below, we will see experimentally that at the maximum self focusing point (with the maximal amplitude), we have $\epsilon|E|^2 \approx 4.6$. Hence, the nonlinear waves with the minimum wavelength of $\lambda_{\text{NL}} \approx \lambda_0/2.4$ are well resolved, with $\lambda_{\text{NL}}/h_z \approx 40$ points per nonlinear wavelength in the z direction, and $\lambda_{\text{NL}}/h_\rho \approx 31$ points per nonlinear wavelength in the ρ direction.[8]

The nonlinearity coefficient was $\epsilon = 0.15$. The parameter that controls the beam collapse in the corresponding critical NLS (4) is the ratio of the incoming beam power $P_0 = \int_0^\infty \rho e^{-2\rho^2} d\rho = \frac{1}{4}$ to the critical power $P_c \approx 1.8623/(\epsilon k_0^2)$, see [35]. For the NLH (19a) with the values of the parameters we have chosen, this power ratio is related to the nonlinearity coefficient ϵ as

$$p = \frac{P_0}{P_c} \approx \frac{\epsilon}{4 \cdot 1.8623} k_0 = 1.29.$$

In Fig. 6(a), we compare the cylindrically symmetric NLH solution with the corresponding NLS solution at the axis of symmetry $\rho = 0$. Since the beam power is 29% above P_c, the solution to the NLS blows up and its on-axis amplitude tends to infinity at $z \approx 5.5$. The corresponding NLH solution, however, remains bounded and its amplitude attains its maximum $\max_{n,m}|E_{n,m}| \approx 5.5$ at $z \approx 6.25$. This yields the maximum Kerr nonlinearity of $\max_{n,m}\{\epsilon|E_{n,m}|^2\} \approx 4.6$.

The square amplitude and energy flux density of the cylindrically symmetric NLH solution are displayed in Fig. 7. As in the "soliton" case, fast oscillations in the z direction are clearly observed for the square amplitude, but not for the energy flux, which appears smooth.

[8] For the soliton simulations in Section 7.1, the nonlinearity was smaller and $\lambda_{\text{NL}} \approx \lambda_0$, so that a separate resolution estimate for λ_{NL} was not needed.

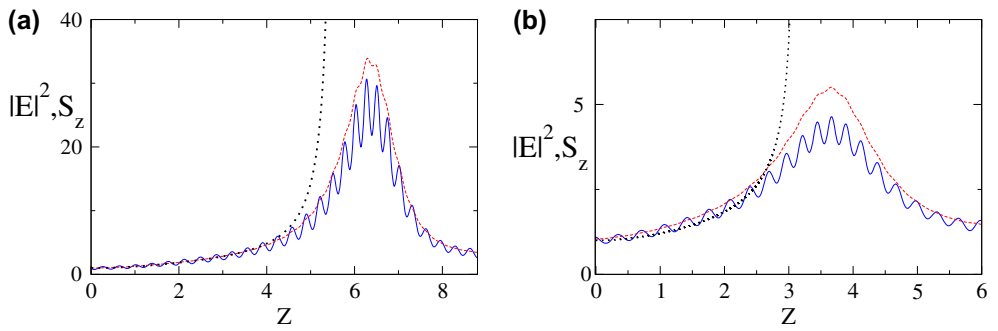

Fig. 6. Arrest of collapse in the NLH: normalized on-axis square-amplitude $|E|^2$ (blue solid), the Poynting vector S_z (red dashed), and the NLS solution (black dotted) on the axis. (a) $D = 3$ and $\sigma = 1$. (b) $D = 2$ and $\sigma = 2$. (For interpretation of the references to color in this figure legend, the reader is referred to the web version of this article.)

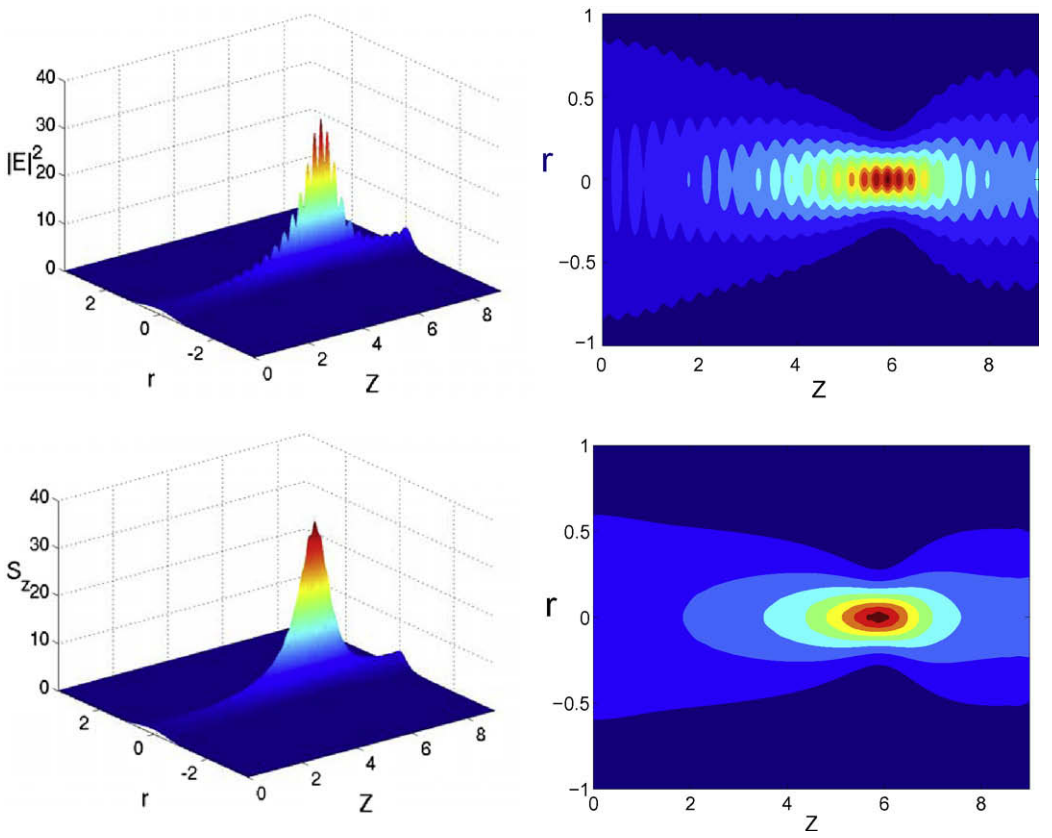

Fig. 7. Arrest of collapse in the cylindrically symmetric NLH. Plots of the square amplitude (top) and the energy flux density (bottom).

7.2.1.1. Grid convergence study. In order to demonstrate the fourth-order grid convergence for the cylindrical geometry case, we conduct a grid convergence study similar to that of Section 7.1.2. For the grids with fewer than roughly 18 points per linear wavelength, the iterations diverge. This is apparently due to insufficient resolution in the region of strong focusing, where it will only be about $18/2.4 = 7.5$ nodes per wavelength. As such, the coarsest grid we have taken had 17.5 points per linear wavelength in the z direction, and the finest grid was $N \times M = 1140 \times 380$, which corresponds to 100 points per linear wavelength in the z direction. The results of the grid convergence study are summarized in Table 2. The convergence rate that we find is $\mathcal{O}(h^{4.88})$, which is even somewhat better than the $\mathcal{O}(h^4)$ theoretical rate.

7.2.1.2. Effect of the domain size. Our simulations show that the convergence of Newton's iterations depends on the domain size, and specifically on the length $Z_{\max}$ of the Kerr material slab. To investigate this dependence, we attempt to solve the $(2+1)D$ NLH for several domain sizes $Z_{\max} = 1, 2, 3, \ldots, 15$. In order to limit possible effects of the transverse boundaries

Table 2
Grid convergence study for the cylindrically symmetric NLH with $\sigma = 1, p = 1.29, Z_{\max} = 9$, and $\rho_{\max} = 3.5$.

(h_z, h_ρ)	$(\frac{\lambda_0}{35}, \frac{\lambda_0}{30})$	$(\frac{\lambda_0}{50}, \frac{\lambda_0}{43})$	$(\frac{\lambda_0}{70}, \frac{\lambda_0}{60})$	$(\frac{\lambda_0}{100}, \frac{\lambda_0}{86})$
$\|E^{(2h)} - E^{(h)}\|_\infty$	3.63	0.965	0.176	0.0225
$\log_2 \|E^{(2h)} - E^{(h)}\|_\infty$	1.86	−0.051	−2.51	−5.47

Table 3
Convergence of Newton's method for the cylindrically symmetric NLH with $\sigma = 1, k_0 = 8$, and $\epsilon = 0.15$ on the series of domains with $Z_{\max} = 1, 2, \ldots, 15$ and $\rho_{\max} = 5$. The criterion of convergence is $|\delta E^{(j)}| < 10^{-12}$ and $\omega = 0.5$.

$Z_{\max}$	1–3	4–7	8, 9	10–15
Convergence	YES	NO	YES	NO

on the convergence, it was positioned relatively far from the axis, at $\rho_{\max} = 5$. In order to limit possible effects of under-resolution, we have chosen moderate resolutions of $\lambda_0/h_z = 53$ points per linear wavelength in the longitudinal z direction and $\lambda_0/h_\rho = 31$ points per linear wavelength in the transverse ρ direction. The results are displayed in Table 3. It can be seen that for some domain lengths the algorithm converges, while for others it diverges. It may be possible that the divergence observed for the domain lengths between 4 and 7 is related to the boundary $z = Z_{\max}$ being positioned too close to the region of maximum self-focusing, see Fig. 6(a).

7.2.2. The 2D quintic nonlinearity case

We solve the Cartesian NLH (18a) for $\sigma = 2, k_0 = 2\pi/\lambda_0 = 8, \nu = 1, Z_{\max} = 6$, and $X_{\max} = 3$. The problem is driven by the collimated incoming beam $E^0_{\text{inc}}(x) = \frac{1+\sqrt{1+\epsilon e^{-4x^2}}}{2} e^{-x^2}$, for which the refracted beam is approximately a Gaussian: $E^0_{\text{refracted}} \approx e^{-x^2}$, see formula (55). The grid dimension is $N \times M = 900 \times 300$, which translates into the resolution of $\lambda_0/h_z = 120$ grid points per linear wavelength in the z direction and $\lambda_0/h_x = 80$, grid points per linear wavelength in the x direction. The shortest nonlinear wavelength was $\lambda_{\text{NL}} = \lambda_0/\sqrt{1 + \epsilon \max |E|^4} \sim \lambda_0/1.85$. The nonlinear waves are therefore still well resolved, with $\lambda_{\text{NL}}/h_z = 65$ and $\lambda_{\text{NL}}/h_x = 43$. The nonlinearity coefficient was chosen $\epsilon = 0.125$, and the ratio of the incoming beam power was $P_0/P_c \approx 1.30$. The results are displayed in Fig. 6(b), and are similar to the 3*D* cylindrically symmetric critical case.

7.2.3. An inclined beam: focusing–defocusing oscillations

We solve the 2*D* NLH with $\sigma = 2, k_0 = 8$ and $\nu^2 = 1$ on the domain with $Z_{\max} = 12$ and $X_{\max} = 12$ for a Gaussian incoming beam entering the Kerr material at $z = 0, x = 4$ and propagating at the angle of $\pi/5.3$. The nonlinearity coefficient was $\epsilon = 0.12$, which yields the input power of 28% above critical. The grid was $N \times M = 400 \times 800$, which corresponds to resolutions of $\lambda_0/h_z = \lambda_0/h_x = 26$ points per linear wavelength, and 14 points per nonlinear wavelength λ_{NL}.

As shown in Fig. 8, the beam undergoes *two* focusing–defocusing oscillations, which qualitatively agrees with the predictions of the modulation theory for the NLS [17]. This is the first time that two focusing-defocusing oscillations are observed in a critical NLH model.

7.3. The effect of adjusting the incoming beam

As indicated in Section 6, the incoming beam for the NLH needs to be adjusted so that to enable a more accurate comparison of the results with those obtained for the corresponding NLS. In this section, we investigate the difference between the NLH solutions obtained with or without adjusting the incoming beam. Namely, we analyze the critical case $D = 3, \sigma = 1$, and rerun the simulation of Section 7.2.1 with $Z_{\max} = 8.5$ and for the incoming beam $E^0_{\text{inc}} = e^{-\rho^2}$, i.e., without adjusting the incoming beam. The resolutions are $\lambda_0/h_z = 83$ and $\lambda_0/h_x = 67$ points per linear wavelength. The results presented in Fig. 9 show that in this case the collapse occurs later and achieves a smaller maximum self-focusing than for the adjusted incoming beam. The insert of Fig. 9 also shows that near the boundary (after the refraction by the interface) the solution with the adjusted incoming beam is indeed much closer to the corresponding NLS profile.

7.4. Comparison with the previous method

In the nested iteration scheme of [2,20,21], at each outer iteration the Kerr nonlinearity is considered fixed, or frozen, which yields the linear homogeneous variable coefficient equation

$$\left(\Delta + k_0^2 + \epsilon k_0^2 |E^{(j)}|^{2\sigma}\right) E^{(j+1)} = 0. \tag{60}$$

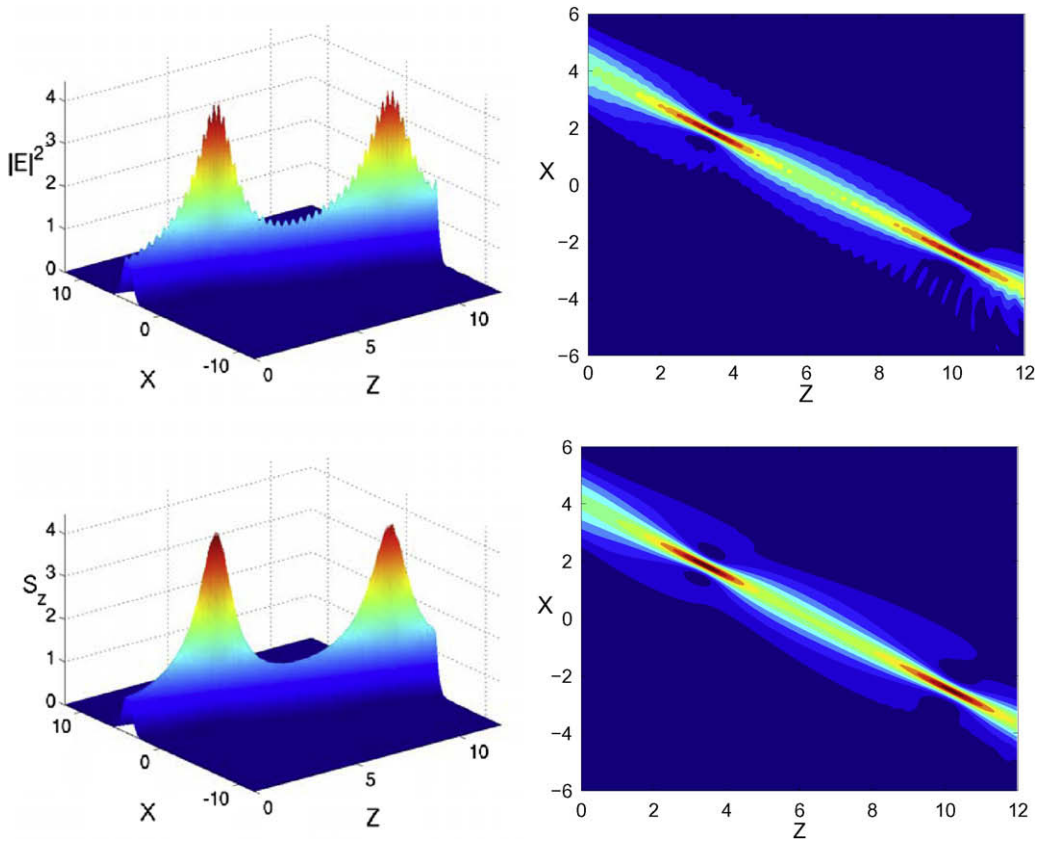

Fig. 8. Arrest of collapse for an inclined beam in the 2D Cartesian NLH. Plots of the square amplitude (top) and the energy flux density (bottom).

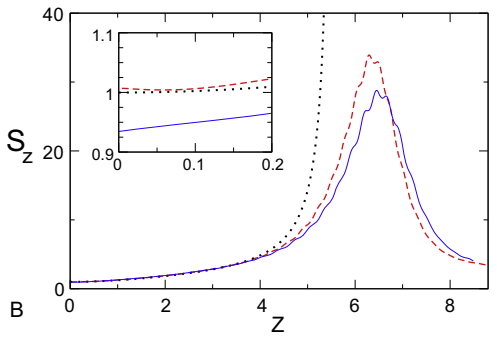

Fig. 9. Comparison of the NLH solutions with and without the adjustment of incoming beam described in Section 6 (dashed red lines and solid blue lines, respectively), and the NLS solution (dotted black line). (For interpretation of the references to color in this figure legend, the reader is referred to the web version of this article.)

Eq. (60) is also solved iteratively, by building a sequence of Born approximations. In doing so, at each inner iteration an inhomogeneous linear constant coefficient equation

$$\left(\Delta + k_0^2\right) E^{(j+1,k+1)} = -\epsilon k_0^2 |E^{(j,K)}|^{2\sigma} E^{(j+1,k)} \tag{61}$$

is solved using the separation of variables. We will call this approach the "nested iterations method".

The efficacy of this method can be improved by getting rid of the inner iterations (61) and solving Eq. (60) by the Gaussian elimination. We will call this the "freezing iterations method".

In the one-dimensional case of [19], the freezing iterations diverged above a certain nonlinearity threshold, while Newton's iterations converged for the entire range of nonlinearities of interest.

Table 4
A comparison of the efficacy of the three methods for the soliton case $D = 2,\ \sigma = 1$. Each method converges for $Z_{\max} < Z_{\max}^{\text{threshold}}$ and diverges for $Z_{\max} \geqslant Z_{\max}^{\text{threshold}}$.

Method	nested freezing (60), (61)	freezing (60), LU solver	Newton's
$Z_{\max}^{\text{threshold}}$	42	135	> 500

In the current multi-D cases that correspond to the critical NLS, i.e., $D = 3, \sigma = 1$ and $D = 2, \sigma = 2$, both the nested iterations method and the freezing iterations method diverge when the NLS solution collapses, i.e., when the input power is above P_c, while Newton's algorithm converges, at least for some configurations, thereby showing a much better efficacy.

Another case of interest from the standpoint of applications is the subcritical NLS, $D = 2, \sigma = 1$, which admits solutions in the form of spatial solitons. To compare the three methods in this case, we use each of them to repeat the simulation of Section 7.1.1 while varying the domain size $Z_{\max}$. The quantity of interest is the threshold value $Z_{\max} = Z_{\max}^{\text{threshold}}$, below which a given solver converges and above which it diverges. The results are given in Table 4. We can see that the nested iterations method of [2,20,21] converges only for relatively short domains $Z_{\max} < Z_{\max}^{\text{threshold}} = 42$. Replacing the inner iteration by a direct solver brings along a certain improvement: $Z_{\max} < Z_{\max}^{\text{threshold}} = 135$. However, similarly to the one-dimensional case, Newton's iterations converge for the widest selection of cases, at least until $Z_{\max} = 500$. Moreover, this limit is due to the memory constraints rather than divergence, and the actual $Z_{\max}^{\text{threshold}}$ may be even larger.

8. Discussion and future plans

In this study, we propose a novel numerical method for solving the scalar nonlinear Helmholtz equation, which governs the propagation of linearly polarized monochromatic light in Kerr dielectrics. The NLH is the simplest model in nonlinear optics that allows for the propagation of electromagnetic waves in all directions and, in particular, for backscattering, and accounts for nonparaxial effects. Our key result is that the NLH eliminates the singularity that characterizes solutions of the nonlinear Schrödinger equation, which is a reduced model based on the paraxial approximation. Another important finding is the discovery of narrow nonparaxial solitons and the development of numerical capability for simulating their collisions.

Mathematically, the NLH is an elliptic equation, and must be solved as a nonlinear boundary-value problem. This presents additional difficulties for both analysis and computations compared to the traditional treatment based on the NLS. The latter has a predominant direction of propagation and requires a Cauchy problem. Physically, we consider the propagation of laser light in a layered medium with interfaces across which both the linear and nonlinear components of the refraction index may undergo jumps. The presence of material discontinuities necessitates setting the condition that the field and its first normal derivative be continuous at the interface.

To solve the NLH numerically, we develop a fourth-order finite difference scheme for one, two, and three space dimensions (in the latter case we assume cylindrical symmetry). Finite differences are chosen over other possible approximation strategies because of their simplicity and ease of implementation. Indeed, the geometry of the problem enables a straightforward discretization on a uniform rectangular grid. On the other hand, having a high order scheme is important because it alleviates the point-per-wavelength constraint for large domains and also helps resolve the small-scale phenomenon of backscattering. In particular, high order accuracy must be maintained across the material discontinuities. This is achieved by using special one-sided differences. In doing so, to simplify the overall discretization we move the outer boundaries away from the interfaces so that the artificial boundary conditions do not "interfere" with the interface treatment. The scheme used in the interior is of a semi-compact type, it is written on three nodes in the longitudinal direction and five nodes in the transverse direction. Having a compact three-node stencil in the longitudinal direction greatly simplifies both the treatment of the interfaces (no special "near interface" nodes) and the treatment of the outer boundaries (no non-physical evanescent modes). At the same time, a compact stencil in the transverse direction is not required because there are no material discontinuities. This circumstance greatly simplifies the design of the overall scheme.

The second key component of the proposed algorithm is the nonlinear solver, which is based on Newton's method. The simulations of [19] have demonstrated a clear superiority of Newton's method in the one-dimensional case. In this paper, we generalize our Newton's solver to the multi-dimensional case, with the expectation that it will let us solve the NLH for those settings when the NLS breaks down, namely, when the NLS solution becomes singular ($\sigma(D-1) = 2$ with input powers above critical), or when the beam width becomes very narrow in the subcritical case ($D = 2, \sigma = 1$), or when counter-propagating nonparaxial solitons interact.

The Newton's solver that we developed has indeed lived up to the promise. In the critical cases, it enables the central result of this work, which is the discovery of bounded NLH solutions for those cases when the corresponding NLS solution blows up. Physically, it shows that nonparaxiality can suppress the singularity formation and hence arrest the collapse of focusing nonlinear waves. While there may be other physical mechanisms that also help arrest the collapse (neglected along the way when the NLH was derived from the Maxwell's equations), it was not known until now whether the solution becomes regular already in the framework of the scalar NLH model, which is the simplest nonparaxial model that incorporates the backward traveling waves.

Predictions of the NLH in the subcritical case include the existence of narrow nonparaxial solitons, and analysis of the interactions (collisions) of such beams, specifically in counter-propagation. These results may be of relevance to potential applications, e.g., the design of the next generation of all-optical circuits. Note that in our previous work [20] we have already

been able to compute narrow spatial solitons. However, the new method proposed in this paper allows us to do that over much longer propagation distances, see Section 7.4.

Let us also note that a different configuration with counter-propagating solitons has been studied by Cohen et. al. in [22] using a system of coupled NLS equations which approximates the NLH. As, however, mentioned in [22], the coupled NLS model is not problem free as it is neither an initial-value problem nor a boundary-value problem. In contrast, since the NLH is solved as a boundary-value problem, it is a natural mathematical setting for such counter-propagating configurations.

The computational cost of the proposed algorithm still remains relatively high; it is dominated (both in memory and CPU time) by the cost of inverting the Jacobian matrix using a direct method. This cost can be reduced if the LU decomposition is replaced with an iterative method. As, however, the Helmholtz operator subject to the radiation boundary conditions is not self-adjoint, the only viable choice of an iteration scheme will be a method of the Krylov subspace type. For this method to work, the system must be preconditioned, and it is the design of a good preconditioner that will be in the focus of our future work on the linear solver. Several candidate techniques will be investigated, including the constant coefficient Helmholtz operator to be inverted by the separation of variables and a paraxial preconditioner based on the Schrödinger operator.

As far as the dependence of Newton's convergence on the domain size, see Section 7.2.1.2, we attribute it to the generally known "fragility" and, in particular, sensitivity of Newton's convergence to the choice of the initial guess. On one hand, it is intuitively reasonable to expect that if the outer boundary is located in the region of maximum self-focusing, then the iterations may experience difficulties to converge, see Table 3. On the other hand, at the moment we do not have a clear and unambiguous mathematical explanation as to why exactly that happens. We have tried a few simple remedies, such as using a continuation approach in the nonlinearity coefficient ϵ and using a damped NLS solution as the initial guess, but none of those has made a substantial difference. We note that in the one-dimensional case the exact solution was available in the closed form [19] and hence we could at least test Newton's convergence by substituting this exact solution as the initial guess. In multi-D, however, we are not aware of any closed form solutions for the slab of finite thickness and therefore, a similar validation procedure becomes problematic.

The piecewise constant formulation that we have considered in the paper in fact presents no loss of generality, at least from the standpoint of numerical solution. It can be very easily extended to the NLH with piecewise smooth material coefficients $v^2(x)$ and $\epsilon(x)$. All one needs to do is replace the constants v and ϵ in the definition of the scheme with the values at the corresponding grid nodes: $v_{n,m} \equiv v(z_n, x_{\perp,m})$ and $\epsilon_{n,m} \equiv \epsilon(z_n, x_{\perp,m})$. However, while the resulting scheme will approximate the variable coefficient scalar NLH (1) with fourth-order accuracy, the validity of Eq. (1) itself from the standpoint of physics may be in question. Indeed, the derivation of the scalar NLH from Maxwell's equations in the case of variable coefficients introduces additional terms (spatial derivatives of v and $\epsilon|E|^2$) which are not included in Eq. (1).

The layered structure and simple geometry that we have adopted present no substantial loss of generality, because this formulation corresponds to many actual physical (e.g., laboratory) settings. The plain-parallel setup studied in the paper certainly simplifies the discretization. At the same time, we are reasonably confident that the proposed scheme can be generalized to more elaborate geometries without compromising its high order accuracy, which is of key importance. One natural approach to doing that is to use Calderon's projections and the method of difference potentials [36].

From the standpoint of physics, the scalar NLH is certainly not the most comprehensive model. It is rather a reduced model based on a number of simplifications. Most notably, the vector nature of electromagnetic field is not taken into account by the scalar NLH because of the assumption of linear polarization. Vectorial effects, on the other hand, are known to become important close to when the nonparaxiality does, i.e., once the beam width becomes comparable to the carrier wavelength. Moreover, the scalar NLH governs monochromatic fields (continuous-wave laser), whereas the actual fields are always time-dependent (typically, pulses of certain duration). Nonetheless, if the duration of the pulse is sufficiently long (many oscillation periods), then the time-periodic model will provide a good approximation.

To take into account the entire range of relevant physical phenomena one needs, of course, to go back and solve the full nonlinear Maxwell's equations. This, however, is a very challenging computational task and besides, the solutions of full Maxwell's equations may be hard to analyze or verify precisely because of all too many additional physical effects. That's why the analysis of the simplest nonparaxial model (i.e., the NLH) may provide a very useful insight into the relevant physics as, in particular, it allows to study the important phenomenon of nonlinear backscattering.

Given the previous considerations, we believe that in the context of physics, the next most natural and most beneficial extension of the work presented in this paper will be taking into account the vectorial effects. The current work provides a solid foundation for this extension as many key elements of the algorithm, e.g., the nonlocal artificial boundary conditions, will only require technical rather than conceptual changes. On the pure numerical side, in addition to the previously mentioned major modifications to the linear solver, we can consider a number of strategies aimed at further improving the numerical resolution in the regions of foremost interest (e.g., around the maximum self-focusing) while not increasing the overall computational cost. Examples include local grid requirement and/or combined approaches when most of the domain is to be done using the NLS whereas the local area of collision between the solitons is computed using the NLH.

Acknowledgments

The research of G. Baruch and G. Fibich was partially supported by the Israel Science Fund, Grant# 123/08. The research of S. Tsynkov was supported by the US NSF, Grants# DMS-0509695 and # DMS-0810963, and by the US Air Force, Grant# FA9550-07-1-0170.

Appendix A. Continuity conditions at material interfaces

For optical frequencies, we can disregard all magnetization effects in the medium (see [37, Chapter IX]) and write down the time-harmonic Maxwell's equations as follows:

$$\frac{i\omega}{c}B = \mathrm{curl}E, \quad -\frac{i\omega}{c}D = \mathrm{curl}B, \tag{62}$$

where the specific form of how the electric induction D depends on the field E is not important for the derivation of the interface conditions. Note, however, that as our medium is a dielectric, both fields E and B, as well as the induction D, remain finite everywhere including the interfaces.

Let an interface plane be normal to the coordinate z of the Cartesian system (x, y, z). Then, the first equation of (62) implies that the quantity $(\mathrm{curl}E)_x = \frac{\partial E_z}{\partial y} - \frac{\partial E_y}{\partial z}$ is bounded at the interface. As the derivative $\frac{\partial E_z}{\partial y}$, which is taken along the interface, is bounded in its own right, we conclude that $\frac{\partial E_y}{\partial z}$ is bounded. This immediately yields the continuity of E_y across the interface. The continuity of E_x can be established the same way, by taking into account the boundedness of $(\mathrm{curl}E)_y = \frac{\partial E_x}{\partial z} - \frac{\partial E_z}{\partial x}$. Altogether, this means that the tangential component of the electric field E must remain continuous. Likewise, the continuity of the tangential component of B across the interface can be derived by employing the second equation of (62) and the boundedness of D.

Next, consider the case of linear polarization:

$$E = [E_x, 0, 0] \quad \text{and} \quad B = [0, B_y, 0].$$

Then, the continuity of B_y immediately implies the continuity of $\frac{\partial E_x}{\partial z}$, because from the Faraday law (the first equation of (62)) we now have: $\frac{i\omega}{c}B_y = \frac{\partial E_x}{\partial z}$. Altogether, we conclude that for the linearly polarized light propagating through a (transparent) dielectric with material discontinuities, both the electric field E and its first normal derivative must be continuous at all the interfaces.

Appendix B. Notation for central difference operators

We denote the central difference operators by the letter D with the order of differentiation in the subscript and the order of accuracy in the superscript. The full list for the finite differences in the x (or ρ) direction is as follows:

$$D_x^{(2)}E \stackrel{\mathrm{def}}{=} \frac{E_{n,m+1} - E_{n,m-1}}{2h_x} = \partial_x E_{n,m} + \mathcal{O}\left(h^2\right),$$

$$D_{xx}^{(2)}E \stackrel{\mathrm{def}}{=} \frac{E_{n,m+1} - 2E_{n,m} + E_{n,m-1}}{h_x^2} = \partial_{xx} E_{n,m} + \mathcal{O}\left(h^2\right),$$

$$D_{xxx}^{(2)}E \stackrel{\mathrm{def}}{=} \frac{E_{n,m+2} - 2E_{n,m+1} + 2E_{n,m-1} - E_{n,m-2}}{2h_x^3} = \partial_{xxx} E_{n,m} + \mathcal{O}\left(h^2\right),$$

$$D_{xxxx}^{(2)}E \stackrel{\mathrm{def}}{=} \frac{E_{n,m+2} - 4E_{n,m+1} + 6E_{n,m} - 4E_{n,m-1} + E_{n,m-2}}{h_x^4} = \partial_{xxxx} E_{n,m} + \mathcal{O}\left(h^2\right),$$

$$D_x^{(4)}E \stackrel{\mathrm{def}}{=} \frac{-E_{n,m+2} + 8E_{n,m+1} - 8E_{n,m-1} + E_{n,m-2}}{12h_x} = \partial_x E_{n,m} + \mathcal{O}\left(h^4\right),$$

$$D_{xx}^{(4)}E \stackrel{\mathrm{def}}{=} \frac{-E_{n,m+2} + 16E_{n,m+1} - 30E_{n,m} + 16E_{n,m-1} - E_{n,m-2}}{12h_x^2} = \partial_{xx} E_{n,m} + \mathcal{O}\left(h^4\right).$$

Because of the semi-compact approximation we use, only the second-order operator is required in the z direction

$$D_{zz}^{(2)}E \stackrel{\mathrm{def}}{=} \frac{E_{n+1,m} - 2E_{n,m} + E_{n-1,m}}{h_z^2} = \partial_{zz} E_{n,m} + \mathcal{O}\left(h^2\right).$$

References

[1] G. Fibich, B. Ilan, Vectorial and random effects in self-focusing and in multiple filamentation, Physica D 157 (1–2) (2001) 112–146.
[2] G. Fibich, S.V. Tsynkov, High-order two-way artificial boundary conditions for nonlinear wave propagation with backscattering, J. Comput. Phys. 171 (2001) 632–677.
[3] C. Sulem, P.-L. Sulem, The Nonlinear Schrödinger Equation of Applied Mathematical Sciences, vol. 139, Springer-Verlag, New York, 1999.
[4] R.W. Boyd, Nonlinear Optics, third ed., Academic Press, San Diego, 2008.
[5] M.I. Weinstein, Nonlinear Schrödinger equations and sharp interpolation estimates, Commun. Math. Phys. 87 (1983) 567–576.
[6] J.H. Marburger, F.S. Felber, Theory of a lossless nonlinear Fabry–Perot interferometer, Phys. Rev. A 17 (1978) 335–342.
[7] H. Wilhelm, Analytical solution of the boundary-value problem for the nonlinear Helmholtz equation, J. Math. Phys. 11 (1970) 824–826.
[8] W. Chen, D.L. Mills, Optical response of a nonlinear dielectric film, Phys. Rev. B 35 (1987) 524–532.
[9] W. Chen, D.L. Mills, Optical response of nonlinear multilayer structures: bilayers and superlattices, Phys. Rev. B 36 (1987) 6269–6278.
[10] H.V. Baghdasaryan, T.M. Knyazyan, Problem of plane EM wave self-action in multilayer structure: an exact solution, Optical Quant. Electron. 31 (9–10) (1999) 1059–1072.

[11] M. Midrio, Shooting technique for the computation of plane-wave reflection and transmission through one-dimensional nonlinear inhomogeneous dielectric structures, J. Opt. Soc. Am. B – Opt. Phys. 18 (12) (2001) 1866–1871.
[12] P.K. Kwan, Y.Y. Lu, Computing optical bistability in one-dimensional nonlinear structures, Opt. Commun. 238 (1–3) (2004) 169–175.
[13] J. Petráček, Frequency-domain simulation of electromagnetic wave propagation in one-dimensional nonlinear structures, Opt. Commun. 265 (1) (2006) 331–335.
[14] N. Akhmediev, J.M. Soto-Crespo, Generation of a train of three-dimensional optical solitons in a self-focusing medium, Phys. Rev. A 47 (1993) 1358–1364.
[15] N. Akhmediev, A. Ankiewicz, J.M. Soto-Crespo, Does the nonlinear Schrödinger equation correctly describe beam propagation?, Opt Lett. 18 (1993) 411–413.
[16] M. Feit, J. Fleck, Beam nonparaxiality, filament formation and beam breakup in the self-focusing of optical beams, J. Opt. Soc. Am. B 5 (1988) 633.
[17] G. Fibich, Small beam nonparaxiality arrests self-focussing of optical beams, Phys. Rev. Lett. 76 (1996) 4356–4359.
[18] M. Sever, An existence theorem for some semilinear elliptic systems, J. Differen. Equat. 226 (2) (2006) 572–593.
[19] G. Baruch, G. Fibich, S. Tsynkov, High-order numerical method for the nonlinear Helmholtz equation with material discontinuities in one space dimension, J. Comput. Phys. 227 (2007) 820–850.
[20] G. Fibich, S.V. Tsynkov, Numerical solution of the nonlinear Helmholtz equation using nonorthogonal expansions, J. Comput. Phys. 210 (2005) 183–224.
[21] G. Baruch, G. Fibich, S. Tsynkov, Numerical solution of the nonlinear Helmholtz equation with axial symmetry, J. Comput. Appl. Math. 204 (2) (2007) 477–492.
[22] O. Cohen, R. Uzdin, T. Carmon, J.W. Fleischer, M. Segev, S. Odoulov, Collisions between optical spatial solitons propagating in opposite directions, Phys. Rev. Lett. 89 (13) (2002) 133901.
[23] I. Harari, E. Turkel, Accurate finite difference methods for time-harmonic wave propagation, J. Comput. Phys. 119 (2) (1995) 252–270.
[24] I. Singer, E. Turkel, High-order finite difference methods for the Helmholtz equation, Comput. Methods Appl. Mech. Eng. 163 (1–4) (1998) 343–358.
[25] G. Baruch, G. Fibich, S. Tsynkov, E. Turkel, Fourth order scheme for wave-like equations in frequency space with discontinuities in the coefficients, Commun. Comput. Phys. 5 (2-4) (2007) 442–455.
[26] M. Born, E. Wolf, Principles of Optics: Electromagnetic Theory of Propagation, Interference and Diffraction of Light, With contributions by A.B. Bhatia, P.C. Clemmow, D. Gabor, A.R. Stokes, A.M. Taylor, P.A. Wayman, W.L. Wilcock, seventh (expanded) ed., Cambridge University Press, Cambridge, 1999.
[27] F.G. Tricomi, Integral Equations, Dover Publications Inc., New York, 1985, reprint of the 1957 original.
[28] G. Baruch, G. Fibich, S. Tsynkov, Simulations of the nonlinear Helmholtz equation: arrest of beam collapse, nonparaxial solitons and counter-propagating beams, Opt. Exp. 16 (17) (2008) 13323–13329.
[29] P.M. Morse, H. Feshbach, Methods of Theoretical Physics, 2 vols., International Series in Pure and Applied Physics, McGraw-Hill Book Co., Inc., New York, 1953.
[30] M.S. Agranovich, B.Z. Katsenelenbaum, A.N. Sivov, N.N. Voitovich, Generalized Method of Eigenoscillations in Diffraction Theory, Wiley-VCH Verlag Berlin GmbH, Berlin, 1999 (translated from the Russian manuscript by Vladimir Nazaikinskii).
[31] S.V. Tsynkov, Numerical solution of problems on unbounded domains. A review, Appl. Numer. Math. 27 (1998) 465–632.
[32] V.S. Ryaben'kii, Necessary and sufficient conditions for good definition of boundary value problems for systems of ordinary difference equations, USSR Comput. Math. Math. Phys. 4 (1964) 43–61.
[33] J.D. Jackson, Classical Electrodynamics, third ed., Wiley, New-York, 1998.
[34] P. Chamorro-Posada, G. McDonald, G. New, Non-paraxial solitons, J. Mod. Opt. 45 (1998) 1111–1121 (11).
[35] G. Fibich, G.C. Papanicolaou, Self-focusing in the perturbed and unperturbed nonlinear Schrodinger equation in critical dimension, SIAM J. Appl. Math. 60 (1999) 183–240.
[36] V.S. Ryaben'kii, Method of Difference Potentials and Its Applications of Springer Series in Computational Mathematics, vol. 30, Springer-Verlag, Berlin, 2002.
[37] L.D. Landau, E.M. Lifshitz, Course of Theoretical Physics, Electrodynamics of Continuous Media, vol. 8, Pergamon Press, Oxford, 1984.